Low-velocity impact on high-strength steel sheets: an experimental and numerical study

G. Gruben[*], M. Langseth, E. Fagerholt and O.S. Hopperstad

Structural Impact Laboratory (SIMLab), Department of Structural Engineering, Norwegian University of Science and Technology, Rich. Birkelands vei 1A, NO-7491 Trondheim, Norway

---

Abstract

Low-velocity impact tests were performed on dual-phase and martensitic steel sheets and compared with corresponding quasi-static tests. The geometry and loading condition of the specimens were similar to formability tests, and the average strain rates before failure were in the range 80-210 s^{-1} for the low-velocity tests and 0.002-0.005 s^{-1} for the quasi-static tests. For both loading rates, the sheets failed under pre-dominant membrane loading, and by varying the specimen geometry, the stress states prior to failure ranged from uniaxial tension to equi-biaxial tension. Thus, the most important stress states occurring during an impact event in a thin-walled structure are covered. The experiments were complemented by nonlinear finite element simulations, where higher-order solid elements and a refined mesh were applied to capture the failure of the sheets. The materials were modelled using the Hershey high-exponent yield function combined with the associated flow rule and isotropic hardening. Quasi-static tensile and shear tests and tensile tests at elevated strain rates were performed to calibrate the constitutive relation. The results in terms of force-displacement curves and strain histories at critical positions in the specimens were similar for low-velocity and quasi-static loading, independent of material and specimen geometry. This indicates that the quasi-static test gives a good description of the sheet behaviour under low-velocity impact loading. The numerical simulations were found to be in good agreement with the experimental results, and strengthened the experimental finding that all the sheet-impact tests, except the martensitic steel sheet in a state close to equi-biaxial tension, displayed local necking before final fracture.

Keywords: Sheet-impact; advanced high-strength steel; necking; failure

---

1 Introduction

The low-velocity sheet-impact problem is of interest in many engineering applications, such as protection against dropped objects in the design of offshore structures [1], design against

---

[*] Corresponding author. Tel.: + 47-73-59-46-87; fax: + 47-73-59-47-01

E-mail address: gaute.gruben@ntnu.no (G. Gruben).

28 grounding [2] and ship-ship collisions [3] in ship building, and prediction of the onset of
29 necking in the metal forming industry [4].

30 In most of the low-velocity sheet-impact studies reported in the literature, the parameters
31 investigated have been the nose shape, the mass or the impact velocity of the impactor, the
32 position of impact on the target, the boundary conditions of the sheet, or the sheet material,
33 e.g. [5-8]. Common to these studies is that failure occurs locally at the nose of the impactor
34 and the failure mode is typically plugging in the case of a blunt nose and petaling in the case
35 of an ogival nose. Other failure modes, which may occur in sheets exposed to membrane
36 stretching, are local necking and through-thickness shear fracture. However, these failure
37 modes have mainly been studied in the quasi-static regime.

38 Alsos and Amdahl [9] studied the indentation resistance of stiffened and unstiffened panels
39 exposed to quasi-static loading. Simulations with a local instability criterion and large shell
40 elements [10] were able to give a reasonable prediction of failure. Simonsen and Lauridsen
41 [11] presented experimental results on 1 mm steel sheets exposed to quasi-static loading by
42 semi-spherical impactors with various diameters. The sheets were fixed with square,
43 rectangular or circular boundaries, and failed by local necking followed by material fracture.
44 A detailed study on the failure modes in Nakajima formability tests on 1.5 mm thick steel
45 sheets was conducted by Björklund and Nilsson [12]. Local necking occurred before fracture
46 in all the tests, except for those experiencing stress states close to equi-biaxial tension.
47 Hogström et al. [13] observed necking before fracture in formability tests on 4 mm thick
48 mild-steel sheets for stress-states ranging from uniaxial tension to equi-biaxial tension.
49 Usually formability tests on steel sheets exhibit failure by necking rather than fracture, an
50 exception being equi-biaxial tension where the failure mode depends on the material. Stören
51 and Rice [14] proposed a model to predict material instability based on the assumption that
52 this phenomenon appears simultaneously as the initiation of a vertex on the yield surface. This
53 model predicted well failure in several equi-biaxial tension tests reported in literature. An
54 extension of this model introduced by Jie et al. [15], taking into account the strain-rate effect,
55 improved considerably the prediction of failure in formability tests on steel sheets with strain
56 rates around 0.4 s^{-1}.

57 In formability testing, the experimentalist has control of the stress state in the material before
58 failure. However, this type of tests is usually restricted to quasi-static loading conditions. An
59 exception is the study of Walters [16] who performed dynamic Hasek tests on DP780 steel

2

sheets in a drop tower. The tests were carried out to investigate the effect of stress state and strain-rate on the material's ductility. It was found that the influence of strain-rate on the ductility depended on the stress state.

In this study, two experimental programmes were carried out for thin sheets made of either dual-phase steel or martensitic steel. The main experimental programme involved a novel set-up for low-velocity and quasi-static punch tests on sheet metals. The test set-up was designed to obtain sheet failure under membrane loading and to cover stress states within the range of traditional formability tests. This way the most dominant stress states occurring during an impact event are covered. The second experimental programme consisted of materials tests, namely quasi-static and dynamic tension tests and quasi-static shear tests. The sheet-impact tests were studied experimentally and numerically, using the results from the materials tests to calibrate constitutive models for the materials. It was found that the low-velocity and quasi-static sheet-impact tests exhibited similar response, which implies that the quasi-static tests give a good indication of the sheet behaviour during low-velocity impact. Further it was found that all tests failed by local necking, except for the martensitic steel sheet in a state close to equi-biaxial tension which failed by through-thickness shear fracture induced by shear-banding.

2   Materials

Two high-strength steel sheet materials, Docol 600DL and Docol 1400M, were provided from Swedish Steel AB (SSAB). The sheet thickness was 1.8 mm for Docol 600DL and 1.0 mm for Docol 1400M. Docol 600DL is a dual-phase steel with low yield strength and high work hardening. The nominal yield and ultimate stresses are reported from the manufacturer to be in the range from 280 MPa to 360 MPa and from 600 MPa to 700 MPa, respectively [17]. Through heat treatment the material is given a two-phase structure of ferrite and martensite. The ferrite gives good formability, while the martensite provides the strength. Docol 1400M is a cold-reduced and fully martensitic steel with high strength. The manufacturer reports a minimum yield strength of 1150 MPa and nominal ultimate strength between 1400 MPa and 1600 MPa [18]. The high strength is produced by very fast water quenching from an elevated austenitic temperature range. The chemical compositions of the materials are given in Table 1.

3

3 Material tests

To form the basis for constitutive modelling of the materials, a set of material tests was carried out. Uniaxial tension tests were used to provide true stress versus plastic strain curves up to necking and to investigate if the materials display significant plastic anisotropy. Shear tests were used to find the stress-strain behaviour for large strains and to determine the shape of the yield surface. The rate dependence of the materials was determined from split-Hopkinson tension bar tests.

3.1 Uniaxial tension tests

Uniaxial tension tests were carried out under displacement control in a Zwick/Roll hydraulic testing machine with a capacity of 30 kN. The nominal geometry of the specimens are given in Fig. 1(a). The loading rate was 4 mm/min giving a strain rate before necking of $\dot{e}_0 = 1.0 \cdot 10^{-3}\ \mathrm{s}^{-1}$. For both materials, specimens were cut out at 0°, 45° and 90° to the rolling direction in order to investigate in-plane anisotropy. Two successful tests in each loading direction are presented, thus giving a total of 12 tests for the two materials.

To acquire local strain data from the tests, digital image correlation analyses were performed. Before testing, one side of the specimen was spray-painted with a combination of black and white paint, obtaining a high-contrast speckle pattern to improve the optical measurements. The tests were recorded by a Prosilica GC2450 digital camera equipped with 50 mm Nikon lenses at a frequency of 2 Hz. The images were post-processed using an in-house digital image correlation (DIC) software [19], thus producing the displacement fields.

The force, F, was measured by the load cell of the hydraulic actuator, while displacements were collected by a synchronized virtual extensometer with initial gauge length $L_s = 60$ mm based on the DIC measurements, see Fig. 2(a). The engineering stress, s, and the engineering strain, e, were calculated as

$$s = \frac{F}{A_s}, \qquad e = \frac{L}{L_s} - 1 \tag{1}$$

where A_s is the measured initial area of the specimen and L is the extensometer gauge length. The true stress, σ, true strain, ε, and true plastic strain, ε^p, before necking were calculated by standard relations as

4

$$117 \qquad \sigma = s(1+e), \qquad \varepsilon = \ln(1+e), \qquad \varepsilon^p = \varepsilon - \frac{\sigma}{E_m} \qquad (2)$$

118   where E_m is the measured Young's modulus in each test. Fig. 3(a-b) shows the engineering

119   stress-strain curves for the whole loading history of the two materials.

120   To investigate the plastic anisotropy of the materials, the Lankford coefficients and the flow

121   stress ratios were calculated for each test. At a given angle α between the loading direction

122   and the rolling direction, the Lankford coefficient is defined as

$$123 \qquad R_\alpha = \frac{d\varepsilon_W^p}{d\varepsilon_T^p} = -\frac{d\varepsilon_W^p}{d\varepsilon_L^p + d\varepsilon_W^p} \qquad (3)$$

124   where $d\varepsilon_W^p$, $d\varepsilon_T^p$ and $d\varepsilon_L^p$ are the incremental true plastic strains in respectively the width,

125   thickness and longitudinal directions of the specimen. The last equality in Eq. (3) stems from

126   the assumption of plastic incompressibility. Two virtual extensometers were applied to

127   measure the strains in the longitudinal and width directions of the specimen. The gauge length

128   of the extensometers was approximately 150 pixels, which corresponds to 7.2 mm. The true

129   plastic strains ε_L^p and ε_W^p were then calculated using standard relations, and the average

130   Lankford coefficients were determined in the range $0.018 \leq \varepsilon_L^p \leq 0.137$ for 600DL and

131    $0.0027 \leq \varepsilon_L^p \leq 0.012$ for 1400M. The results are summed up in

132   Table 2. The flow stress ratio for an angle α at a specified amount of specific plastic work,

133    $W_p = \int \sigma_\alpha d\varepsilon_\alpha^p$, is defined as

$$134 \qquad r_\alpha = \left. \frac{\sigma_\alpha}{\sigma_0} \right|_{W_p} \qquad (4)$$

135   where σ_0 is the flow stress for $\alpha = 0°$. In this study, σ_0 is defined as the average value from

136   the two parallel tests loaded in the rolling direction. The average flow stress ratios were

137   calculated in the intervals $20 \text{ MPa} \leq W_p \leq 90 \text{ MPa}$ for 600DL and $5 \text{ MPa} \leq W_p \leq 25 \text{ MPa}$ for

138   1400M, and are compiled in

139   Table 2. As can be seen from

5

140 Table 2, both the Lankford coefficients and the flow stress ratios are close to unity for both
141 materials, indicating that the plastic anisotropy of these materials is negligible.

3.2 *In-plane shear tests*

143 The in-plane shear tests were carried out under displacement control in the same Zwick/Roll
144 testing machine. The applied loading rate was 0.3 mm/min corresponding to an initial strain
145 rate in the gauge area of $1.0 \cdot 10^{-3}$ s^{-1}. The geometry of the shear specimen is given in Fig.
146 1(b). Two successful parallel tests for each material are presented. The specimens were cut
147 out with the longitudinal axis in the rolling direction of the sheet. The force level was
148 measured by the load cell of the hydraulic test machine and the displacement was measured
149 by a virtual extensometer, see Fig. 2(b). The gauge length of the shear specimen is 5 mm. To
150 account for differences in the gauge area of the duplicates, a normalized force F/A_s was
151 calculated, where F is the measured force and A_s is the measured initial area of the gauge
152 section. The normalized force versus displacement curves are plotted in Fig. 3(c-d) for the
153 two materials.

3.3 *Split-Hopkinson tension bar tests*

155 Tensile tests at strain rates in the range 200-600 s^{-1} were conducted in a split-Hopkinson
156 tension bar set-up. A detailed description of the experimental set-up and data processing is
157 given by Chen et al. [20]. By using the relations from one-dimensional wave theory, and
158 assuming force equilibrium in the specimen, the engineering stress s and the nominal
159 engineering strain $\bar{e}$ in the specimen are calculated from the transmitted engineering strain e_T
160 and the reflected engineering strain e_R in the bars as

$$161 \qquad s(t) = \frac{E_0 A_0}{A_s} e_T(t), \quad \bar{e}(t) = -2\frac{c_s}{L_s}\int_0^t e_R(t)\, dt \qquad (5)$$

162 where $E_0 = 204$ GPa and $A_0 = 78.54$ mm^2 are the Young's modulus and the cross-section
163 area of the bar, $L_s = 5$ mm is the nominal gauge length, A_s is the measured initial cross-
164 section area of the specimen, and $c_s = 5100$ m/s is the speed of sound in the bars. Since some
165 deformation takes place in the transition part of the specimen, the measured strain is
166 overestimated. A correction was carried out following the method proposed by Albertini and
167 Montagnani [21], and a corrected engineering strain was calculated as

6

168
$$e(t) = \bar{e}(t) - s(t) \cdot \frac{E \cdot E_m}{E - E_m} \tag{6}$$

169 where E_m is the measured Young's modulus and $E = 210\,\text{GPa}$ is used as the correct

170 Young's modulus of the steel sheets. Initially it was planned to calculate the engineering

171 strain from DIC measurements, but the paint came loose during testing and the measurements

172 could not be used. Since the materials under investigation are delivered as thin sheets, the test

173 specimens had to be glued to fixtures. Afterwards the fixtures were threaded and used to

174 fasten the specimen to the steel bars, see [22]. Fig. 1(c) shows the geometry of the test

175 specimen and the fixtures. For comparison, tensile tests at lower strain rates ($\dot{e}_0 = 1.0 \cdot 10^{-3}\,\text{s}^{-1}$

176 and $\dot{e}_0 = 1.0\,\text{s}^{-1}$) were conducted in the Zwick/Roll hydraulic testing machine using the same

177 small-sized specimens. The force and displacement from the load cell in the testing machine

178 were applied in calculating the nominal engineering stress-strain curve for each test. An

179 exception is the 1400M tests with $\dot{e}_0 = 1.0 \cdot 10^{-3}\,\text{s}^{-1}$ where DIC measurements were used to

180 calculate the engineering strain. A gauge length of $L_s = 5\,\text{mm}$ was applied to derive the

181 engineering strain, and the nominal engineering strain from the load cell measurements was

182 corrected for machine stiffness by use of Eq. (6).

183 The results in terms of engineering stress-strain curves for various strain rates are shown in

184 Fig. 3(e-f). Clearly both materials display an increase in flow stress for increasing strain rate.

185 The dynamic SHTB tests on the dual-phase steel do not display a large scatter in stress level,

186 while one of the dynamic SHTB tests on the martensitic steel is significantly lower than the

187 other tests and is considered to be an outlier. Both materials display oscillations for low strain

188 levels. However, only the flow stresses at equivalent plastic strain equal to 10 % and 15 % for

189 Docol 600DL and 1.5 % for Docol 1400M are to be further used from these tests. The flow

190 stress as a function of plastic strain-rate at the aforementioned plastic strains is shown in Fig.

191 4(a-b) for the two sheet materials. For both materials, the flow stress displays a logarithmic

192 increase with strain rate, and by increasing the strain rate from $10^{-3}\,\text{s}^{-1}$ to $10^2\,\text{s}^{-1}$ an

193 approximate increase of 70 MPa is observed.

194 The dynamic SHTB tests are nearly adiabatic, and the temperature increase, ΔT, in the

195 specimen during testing can be estimated as

7

196
$$\Delta T = \chi \frac{W_p}{\rho C_p} \tag{7}$$

197 where $\chi = 0.9$ is the Taylor-Quinney coefficient, $\rho = 7850$ kg/m^3 is the density of the steel

198 specimens, $C_p = 450$ J/(kg$\cdot$K) is the specific heat of the steel specimens, and W_p is the

199 specific plastic work as defined previously. At diffuse necking, W_p is approximately

200 120 MJ/m^3 for the 600DL tests and 35 MJ/m^3 for the 1400M tests. According to Eq.(7), this

201 indicates an increase in temperature of approximately 30°C and 9°C at diffuse necking for the

202 600DL and 1400M tests, respectively. Consequently, the influence of temperature on the

203 material behaviour before diffuse necking, and thus on the results in Fig. 4, can be neglected.

204 By comparing the engineering stress-strain curves from the quasi-static tensile tests on the

205 small SHTB-type specimens $(\dot{e}_0 = 1.0 \cdot 10^{-3}$ s$^{-1})$ in Fig. 3(e-f) with those on the large

206 specimens in Fig. 3(a-b), an apparent size effect is disclosed. At necking, the tests on the

207 smaller SHTB-type specimens give 3-4% lower stresses than the tests on the larger

208 specimens. It is emphasized that before necking both specimen types are in uniaxial tension

209 with strain rates close to the nominal values, and the specimens were cut from neighbouring

210 positions in the centre of the delivered steel sheets. The reason for this apparent size effect is

211 not known, but it does not influence the results from the strain-rate tests in Fig. 4 as these are

212 performed on the same type specimens.

213 **4 Constitutive model**

214 The elastic properties of the materials were described by a Young's modulus of 210 GPa and

215 a Poisson ratio of 0.3, while the material density was set to 7850 kg/m^3. Due to the almost

216 isotropic behaviour of both materials, the high-exponent Hershey yield function [23] with

217 associated plastic flow and isotropic work hardening was found appropriate. The dynamic

218 yield criterion is given as

219
$$f = \sigma_{eq} - Y = 0 \tag{8}$$

220 where σ_{eq} is the equivalent stress and Y is the flow stress. The equivalent stress is defined by

221
$$\sigma_{eq} = \sqrt[m]{\frac{1}{2}\left((\sigma_I - \sigma_{II})^m + (\sigma_{II} - \sigma_{III})^m + (\sigma_I - \sigma_{III})^m\right)} \tag{9}$$

8

222   where $\sigma_I \geq \sigma_{II} \geq \sigma_{III}$ are the ordered principal stresses and m is an exponent controlling the

223   shape of the yield surface. For $m = 2$ and $m = 4$, the von Mises yield surface is obtained,

224   while $m \to 0$ and $m \to \infty$ gives the Tresca yield surface. According to Logan and Hosford

225   [24], $m = 6$ is a good approximation for BCC materials, and this was confirmed for both steel

226   sheets during the calibration process. The flow stress is defined by [25]

$$Y = \left(\sigma_0 + \sum_{i=1}^{3} Q_i \left(1 - \exp(-C_i p) \right) \right) \cdot \left(1 + \frac{\dot{p}}{\dot{\varepsilon}_0} \right)^c \tag{10}$$

228   where $\dot{p}$ is the equivalent plastic strain-rate, $p = \int \dot{p} dt$ is the equivalent plastic strain, σ_0 is

229   the yield stress, and Q_i and C_i $(i = 1, 2, 3)$ are parameters governing the work hardening. The

230   parameters c and $\dot{\varepsilon}_0$ define the strain-rate sensitivity of the material. The equivalent plastic

231   strain-rate is defined by $\dot{p} = \boldsymbol{\sigma} : \mathbf{D}^p / \sigma_{eq}$, where $\boldsymbol{\sigma}$ is the Cauchy stress tensor and $\mathbf{D}^p$ is the

232   plastic rate-of-deformation tensor defined by the associated flow rule.

233   The test results from the split-Hopkinson bar tests were used to determine the parameters c

234   and $\dot{\varepsilon}_0$, and the resulting curve fits are shown in Fig. 4(a) and (b). The other material

235   parameters were found by use of inverse modelling of the tensile and shear tests.

236   To this end, the nonlinear finite element (FE) solver IMPETUS Afea [26] was used; the

237   response parameters being the engineering stress-strain curves from the tensile tests and the

238   normalized force-displacement curves from the shear tests. The specimens were discretized

239   by fully integrated hexahedral elements with cubic shape functions, see Fig. 5. An in-plane

240   element size of approximately 0.95 mm was found sufficient to give a good description of the

241   diffuse and local necking phenomena in the tensile specimens. The shear specimens were not

242   exposed to significant local necking, but the large deformations occurring over the relatively

243   small gauge area required a resolution with an in-plane element size of 0.27 mm. To reduce

244   the number of elements, a symmetry plane in the thickness direction was applied; this is

245   illustrated in Fig. 5(b) for the shear specimen. Two elements were used over half the thickness

246   for both the tensile and shear specimens. As IMPETUS Afea is an explicit FE code, mass

247   scaling was applied to reduce the computational time. To evaluate the mass scaling effect,

248   several simulations of the uniaxial tensile test for the 600DL material were run with

249   decreasing mass scaling factor. Mass scaling by a factor $4.0 \cdot 10^8$ was found to have only

250   minor influence on the diffuse and local necking predictions. After all simulations, it was

9

251 carefully checked that the kinetic energy remained a small fraction of the internal energy of
252 the specimen. In the simulations of the tensile tests, prescribed velocities were applied to rigid
253 parts at an appropriate distance away from the gauge region, see Fig. 5(a). The prescribed
254 velocity was ramped up over the first 30 seconds using a smooth transition function. In the
255 simulations of the shear tests, the nodal displacements from a DIC analysis of one duplicate
256 were imposed directly to the finite element mesh, see Fig. 5(c). The nodal displacements were
257 applied to two parts that were discretized with trilinear elements and merged with the cubic
258 elements used in the central part of the specimen. It was assumed that the displacement was
259 homogenous through the thickness of the specimen. The results from the final simulations are
260 shown in Fig. 3(a-d). The constitutive material parameters for both materials are summed up
261 in

262 Table 3.

263 To validate the material model for high strain-rate conditions, simulations of the SHTB tests
264 were run. The specimens were discretized with cubic elements with an in-plane size of
265 0.25 mm and two elements over half the thickness in the necking region. A symmetry plane
266 was applied in the thickness direction. The boundary conditions were prescribed velocities
267 applied to rigid parts at an appropriate distance away from the gauge region, see Fig. 5(d). In
268 addition to the dynamic tests in the SHTB with nominal strain rate 200 s^{-1}, the quasi-static
269 tests on the same type of specimens with nominal strain rate 0.001 s^{-1} were simulated.
270 Similar to the experimental data processing, the displacement at the boundaries (rigid parts),
271 were applied to calculate the nominal engineering strain, which was subsequently corrected
272 according to Eq.(6).

273 The simulated engineering stress-strain curves are shown in Fig. 3(e-f). For both materials,
274 the ultimate stress in the quasi-static simulations, Fig. 3(e-f), is similar to the ultimate stress in
275 the simulations of the large specimens, Fig. 3(a-b). This indicates that the size effect observed
276 in the experiments is not only related to the geometry of the specimens. Since the calibration
277 of the material model is based on the results from the larger uniaxial tension specimen, and
278 the apparent size effect is only present in the experiments, both the quasi-static and dynamic
279 simulations with the small specimen display higher engineering stress levels than their
280 corresponding experiments as shown in Fig. 3(e-f).

281 Considering the dynamic simulations, the post-necking part of the 1400M engineering stress-
282 strain curve displays the same slope as the dynamic experimental curves, see Fig. 3(f). For the

10

283 600DL material, the post-necking stress level in the simulation actually drops more rapidly

284 than in the experiments, as can be seen in Fig. 3(e). Although a temperature increase up to as

285 much as 150°C-200°C can be expected locally at the position of fracture initiation, accurate

286 engineering stress-strain curves to failure were obtained numerically without introducing

287 thermal softening in the constitutive model. However, it is noted that the influence of

288 adiabatic heating may depend on the material as well as the stress state during plastic

289 deformation. For instance, Roth and Mohr [27] presented un-notched and notched tensile tests

290 made from 1.4 mm thick dual-phase steel sheets exposed to high strain-rate loading, and

291 found that a temperature independent material model did not provide a good post-necking

292 force-displacement response for all of the tests.

5   Punch tests on sheet metals

294 Low-velocity sheet impact tests were carried out on specimens made from the two materials.

295 To perform the tests, a test rig was designed involving steel rings for clamping of the

296 specimen and an arrangement for monitoring the deformation of the surface of the specimen

297 by use of high-speed cameras, see Fig. 6(a-b). A mirror positioned inside a cylinder with cut

298 outs, Fig. 6(a), was applied. Direct recording of the specimen was not practical since the

299 cylinder was attached to the reaction wall. The mirror was not in direct contact with the

300 cylinder during the impact tests in order to avoid disturbance. The specimens had three

301 different geometries named S20, S100 and S150, see Fig. 6(c), where the number indicates

302 the width in mm in the gauge region. The chosen geometries represent the whole range of

303 stress states in traditional metal formability tests from uniaxial tension (S20) to equi-biaxial

304 tension (S150). The S100 geometry is designed to be close to plane-strain tension, a stress

305 state giving low ductility for many materials [28-30]. In addition to the low-velocity tests, a

306 test series with quasi-static loading was completed to study the effect of the loading rate.

307 During testing, the specimen was clamped between two steel rings, as illustrated in Fig. 6(d).

308 The clamping rings had an inner radius of 75 mm, Fig. 6(e), and the ring facing the cylinder

309 had a rounded edge towards the specimen, see Fig. 6(f). The rounded edge had a smooth

310 surface, while the faces on the rings that were in contact with the specimen had a rough

311 surface to enhance the clamping, see Fig. 6(g). In order to fasten the rings, M16 bolts were

312 used. For the S20 and S100 geometry, 10 bolts were applied, while 16 bolts were applied for

313 the S150 geometry. The bolts were fastened with a torque wrench set to 200 Nm. The cylinder

314 supporting the rings and the specimen was designed so that no plastic deformation would

11

315 occur during testing and so that the surface of the specimen could be monitored easily by the

316 cameras. The cylinder was welded to a steel-plate that easily could be fixed to a rigid support.

317 Details of the cylinder and the mounting steel-plate are shown in Fig. 6(h).

318 The loading was applied by a punch with a hemispherical nose having a radius of 50 mm, as

319 illustrated in Fig. 6(a). The deformation of the specimen was recorded by two cameras via the

320 mirror inside the cylinder that supported the rings and the specimen; see Fig. 6(a-b). The side

321 of the specimen facing the punch was sprayed with a lubricant (Klüber Unimoly C220) to

322 reduce friction, while the side facing the mirror was spray painted with a speckle pattern to

323 enhance the optical measurements. The in-plane logarithmic principal strains and the strain

324 magnitude on the surface of the specimens were determined from the DIC displacement

325 fields. The strain magnitude at a given point is here defined as

$$326 \qquad \varepsilon_e = \sqrt{\frac{2}{3}\left(\varepsilon_1^2 + \varepsilon_2^2 + \varepsilon_3^2\right)} \qquad (11)$$

327 where $\varepsilon_1 = \ln \lambda_1$ and $\varepsilon_2 = \ln \lambda_2$ are the in-plane logarithmic principal strains, λ_1^2 and λ_2^2 being

328 the eigenvalues of the right Cauchy-Green deformation tensor, and $\varepsilon_3 = -\left(\varepsilon_1 + \varepsilon_2\right)$ is the

329 logarithmic principal strain in the thickness direction of the sheet. Plastic incompressibility

330 and negligible elastic strains are assumed. The discretization in the DIC analysis was

331 restricted by the resolution of the high speed cameras and a nodal spacing of 3.5 mm were

332 applied.

5.1 Low-velocity tests

334 The low-velocity impact tests were carried out in a pendulum impactor [31]. Fig. 7(a) shows

335 the schematic set-up of the pendulum impactor. Fig. 7(b) shows how the specimen is

336 positioned in front of the reaction wall. A trolley equipped with a load cell and the punch, see

337 Fig. 7(c), which had a total mass of 417.5 kg, was accelerated to a velocity $v_0 = 10.5$ m/s

338 before impact. Three duplicates were conducted of each test. The recordings in one of the

339 600DL-S20 and 600DL-S150 duplicates failed and are not reported. The time duration from

340 initial contact to fracture was between 1.7 ms (for 1400M-S20) and 4.5 ms (for 600DL-S150).

341 The load cell recorded the force $P(t)$ at 200000 Hz resulting in between 340 and 900 data-

342 points for each test. The recording by the load cell was triggered when the front of the trolley

343 passed a photocell positioned 260 mm ahead of the specimen. This photocell and another one

12

344   positioned 10 mm ahead of the specimen were used to measure the impact velocity of the

345   trolley. The measured impact velocity was in the range $10.45 \text{ m/s} \leq v_0 \leq 10.58 \text{ m/s}$ in the

346   various tests.

347   Under the assumption that the trolley, the load cell and the punch had identical acceleration

348   equal to $\ddot{u}(t)$, the force between the punch and the specimen $F(t)$ were found from

349   Newton's second law as

350
$$
\left. \begin{array}{l} F(t) = (M_T + M_P)\ddot{u}(t) \\ P(t) = M_T\ddot{u}(t) \end{array} \right\} \quad \Rightarrow \quad F(t) = \left(1 + \frac{M_P}{M_T}\right)P(t) \tag{12}
$$

351   Here, $M_T = 385 \text{ kg}$ is the mass of the trolley and the back-part of the load cell, and

352    $M_P = 32.5 \text{ kg}$ is the mass of the punch and the front part of the load cell, see Fig. 7(d).

353   Notably, Eq. (12) predicts that the force between the punch and the specimen is 8.4 % larger

354   than the measured force in the load cell. The velocity $\dot{u}(t)$ and the displacement $u(t)$ were

355   calculated from the force measurements as

356
$$
\dot{u}(t) = v_0 - \int_0^t \frac{P(t)}{M_T} dt
$$
$$
u(t) = \int_0^t \dot{u}(t)\, dt \tag{13}
$$

357   Since the initial kinetic energy is much larger than the dissipated work during impact, the

358   displacement $u(t)$ is nearly a linear function of time.

359   The out-of-plane displacement of the specimen was also obtained from DIC analysis. Here

360   two synchronized Phantom v1610 high speed cameras equipped with 105 mm lenses recorded

361   the deformation of the specimen via the mirror at a framing rate of 21000 Hz, thus resulting in

362   between 36 and 95 images for each test. The positions of the two cameras were approximately

363   0.5 m below the mirror, see Fig. 7(b). The images of one of the 1400M-S20 duplicates were

364   of too low quality for DIC analysis. The displacements obtained from the load cell

365   calculations, using Eq.(13), and the DIC analysis were in agreement. A Photron SA1.1 high-

366   speed camera recorded the impact event from a position normal to the impact direction. The

367   framing rate was 800 Hz, thus giving between 14 and 36 images in each test. The images from

368   the Photron camera were used to check that the steel rings with the specimen mounted were

13

369   not exposed to rigid body motion during loading. No significant rigid body motions were

370   observed during any of the tests. Both the Phantom cameras and the Photron camera were

371   triggered by the same photocell used to trigger the load cell recordings, but the three

372   recordings were not entirely synchronized as the time lag was slightly different for the three

373   devices.

5.2   Quasi-static tests

375   The quasi-static tests were carried out in an Instron 1332 hydraulic testing machine with a

376   capacity of 250 kN. The set-up was mounted vertically as shown in Fig. 8, with the punch

377   moving downwards onto the specimen. The loading was under displacement control with a

378   loading rate of 0.3 mm/s. The hydraulic testing machine recorded the crosshead displacement

379   and the force in a load cell placed above the crosshead. In addition, two Prosilica GC2450

380   cameras equipped with 28-105 mm Nikon lenses were recording the deformation in the gauge

381   area at a framing rate of 2 Hz for the 600DL material and 4 Hz for the 1400M material. The

382   cameras were positioned approximately 1 m from the mirror, see Fig. 8, and the camera

383   recordings were synchronized with the recording of the load cell. Two duplicates per

384   geometry for each material were conducted, thus resulting in a total of 12 quasi-static tests.

385   The images of one of the 600DL-S20 duplicates were of too low quality for DIC analysis.

5.3   Results

387   The results in terms of force-displacement curves for both the low-velocity and the quasi-

388   static tests are given in Fig. 9. All tests display an initially low increase in force level since

389   membrane stresses are not significantly present at low punch displacement, thus the initial

390   reaction force stems from the bending stiffness of the specimen. Both the low-velocity and the

391   quasi-static impact tests display good repeatability. For the 600DL material, the force level is

392   generally higher in the low-velocity tests; this is attributed to the positive strain-rate

393   dependence. For the 1400M material, the force levels in the low-velocity and the quasi-static

394   impact tests are of the same magnitude. Oscillations can be seen in the low-velocity tests,

395   these may stem from a combination of stress waves and dynamic effects as the eigenperiods

396   of the clamped specimens are comparable to the loading time. At failure, a significant drop in

397   the force curve is observed.

398   It was observed to a various degree in all experiments that the location with the largest

399   deformation changed during testing. Initially most deformation occurred in the centre of the

400   specimen, for then gradually to translate radially until necking or fracture occurred. This is

14

401   illustrated in Fig. 10 by the evolution of the strain magnitude measured by DIC on the surface

402   of the quasi-static 600DL-S20 test. This observation implies that the point with the largest

403   strain-rate is moving during loading. Further, DIC measurement of the strain magnitude in the

404   last image before fracture ε_e^f was collected. Fig. 11 shows contour plots of ε_e^f for a selected

405   duplicate of each test. With ε_e^f values in the range 0.41-0.67, the 600DL material shows a

406   significantly more ductile behaviour than the 1400M material, which displays ε_e^f values in

407   the range 0.14-0.41. A tendency, particularly observed in the S20 geometries, is that the low-

408   velocity tests display equally large strain concentrations on both sides of the centre of the

409   specimen, while in the quasi-static tests the strain concentration on one side is dominant. This

410   tendency was also observed in the post-fracture specimens, selected duplicates are shown in

411   Fig. 12. Here a distinct local necking (diffuse necking for 600DL-S20) is present in regions

412   not exposed to fracture in some of the low-velocity specimens, marked with an ellipse, while

413   a similar distinct necking is not observed in the quasi-static tests. The crack started to

414   propagate in the rolling direction in the S150 tests, except in the low-velocity tests of the

415   1400M material. In the S100 and S20 tests, the rolling direction coincided with the direction

416   of the major principal stress, and fracture occurred normal to the rolling direction, except in

417   the 1400M-S20 tests where fracture followed the local neck which appeared approximately

418   64° to the rolling direction.

419   In order to study the failure mode, the thickness in the fracture zone, t_f, and the thickness

420   1.5 mm from the fracture zone, $t_{1.5}$, were measured for each test. Failure is here defined as the

421   incipient necking or onset of fracture, whichever comes first. The measurements were carried

422   out on light microscopy images of selected tests, see Fig. 13. The positions of the

423   measurements are illustrated for one case in Fig. 13. The values of t_f, $t_{1.5}$ and $t_f / t_{1.5}$ are

424   summed up in

425   Table 4. All of the selected tests of the dual-phase material display $t_f / t_{1.5}$ ratios around 0.6,

426   suggesting that the tests fail due to necking. From Fig. 13 it can be seen that shear lips are

427   present in the 600DL tests, indicating that shear banding occurs prior to fracture. For the

428   martensitic material, the S20 geometry display $t_f / t_{1.5}$ ratios around 0.5, while the S100 and

429   S150 geometries display $t_f / t_{1.5}$ ratios around 0.8. This indicates that the S20 geometry fails

430   due to necking, while the S100 and S150 geometries fail due to through-thickness shear

431   fracture. For both materials the low-velocity and quasi-static loading conditions give

15

432   comparable results. Further, the S20 and S100 tests display comparable values of $t_{1.5}$ for both
433   steel sheets, while the S150 tests are exposed to more thinning.

434   The principal strain histories were collected from the DIC element closest to the spatial
435   fracture-initiation point, and Fig. 14 shows ε_1 - ε_2 plots from the tests. The principal strain
436   history and the principal strains from the last image before fracture are approximately the
437   same in the low-velocity and quasi-static tests. It is found that the S20 tests are close to
438   uniaxial tension $(\varepsilon_2 / \varepsilon_1 = -0.5)$, the S100 tests are close to plane-strain tension $(\varepsilon_2 / \varepsilon_1 = 0)$,
439   and the S150 tests are close to equi-biaxial tension $(\varepsilon_2 / \varepsilon_1 = 1)$. The strain paths in uniaxial
440   tension (UT), plane-strain tension (PST) and equi-biaxial tension (EBT) are shown with black
441   thick lines in Fig. 14.

6   Numerical simulations of sheet impact tests

6.1   Modelling of the sheet impact tests

444   A detailed numerical analysis of the impact tests was conducted using the explicit finite
445   element solver IMPETUS Afea.

446   Fully integrated hexahedral elements with cubic shape functions were used to discretize the
447   test specimens, while the material behaviour was described by the constitutive model
448   presented in Section 4. A denser mesh with an in-plane element size of 0.625 mm and two
449   elements in the thickness direction was applied in the regions exposed to the largest
450   deformations, see Fig. 15(a). To provide accurate boundary conditions, the steel rings
451   clamping the specimen were modelled as rigid parts constrained in all translational degrees of
452   freedom, and the nodes on the edges of the specimen were fixed in the in-plane translational
453   degrees of freedom, as shown in Fig. 15(a). In the contact between the specimen and the steel
454   rings, a Coulomb friction coefficient of 0.4 was applied.

455   To ensure similar mechanical impedance in the simulations and the experiments, detailed
456   models of the impacting parts were applied, as shown in Fig. 15(b). The impacting parts were
457   discretized with trilinear hexahedral elements, except for the punch nose that was discretized
458   by tetrahedral elements with cubic shape functions to provide a smooth contact surface. A
459   Coulomb friction coefficient of 0.1 was applied in the punch-specimen contact. According to
460   [32], the friction coefficient for greasy steel-steel surfaces is in the range 0.029-0.12. Two
461   simulations of the low-velocity 600DL-S20 test were run with a friction coefficient of 0.025

16

462 and 0.1. The simulation with friction coefficient equal to 0.1 gave a force-displacement curve

463 in good agreement with the experiment and this value was used in all further simulations. The

464 impacting parts were mainly made of steel with an assumed Young's modulus of 210 GPa, a

465 Poisson ratio of 0.3 and a density of 7850 kg/m^3. The trolley was partly made of aluminium,

466 see Fig. 15(b), and the aluminium was assumed to have a Young's modulus of 70 GPa, a

467 Poisson ratio of 0.3 and a density of 2700 kg/m^3. The constitutive behaviour of the impacting

468 parts was given by linear elastic material models with the above mentioned properties. The

469 force and the displacement were derived from the force $P(t)$ acting in the centre of the load

470 cell by applying Eq.(12) and Eq.(13).

471 In the quasi-static simulations, a node set covering the back of the punch was given a

472 prescribed motion in the loading direction, smoothly ramped up to 0.3 mm/s over the first

473 6.6 s of the simulation. The contact force between the punch and the specimen and the

474 displacement of the apex of the punch-nose were collected for the force-displacement curves.

475 To reduce computational costs, mass scaling was introduced by restricting the maximum time

476 step to $1.3 \cdot 10^{-3}$ s for the 600DL simulations and $5.85 \cdot 10^{-4}$ s for the 1400M simulations.

6.2   Results

478 The simulated force-displacement curves are shown for the low-velocity tests in Fig. 16 and

479 for the quasi-static tests in Fig. 17. The simulations were run without any fracture criterion

480 and thus the drop in force level is due to necking. The quasi-static and low-velocity

481 simulations of the 600DL material display good agreement with the experimental force-

482 displacement curves, which suggests that the constitutive model and the boundary conditions

483 are appropriate. The simulated drop in force level occurs at approximately the same

484 displacement as in the experiments, which supports the experimental finding that these tests

485 are experiencing necking before fracture. The simulated force-displacement curves of the

486 1400M material are in close agreement with the experimental curves, but the drop in the force

487 level occurs at a larger displacement than in the experiments, particularly for the S20 and

488 S150 geometries.

489 As a more local measure of the onset of necking, the element exposed to the largest

490 deformation in each simulation was identified and a local necking criterion was applied based

491 the strain-rate in this critical element and in two neighbouring elements located further away

492 from the centre of the specimen in the radial direction. Fig. 18(a) illustrates the positions of

493 the critical and the neighbouring elements just after necking in the quasi-static 600DL-S20

17

494   simulation. Three elements covering a strip of 1.9 mm and with a total of $n_i = 192$ integration

495   points were found sufficient as the spatial region for the necking prediction in this analysis.

496   The equivalent plastic strain-rate histories from the integration points, $\dot{p}_i(t)$, $i = 1, 2, .., n_i$, were

497   collected and the mean strain-rate history, $\dot{p}_{\mathrm{mean}}(t) = n_i^{-1} \sum_1^{n_i} \dot{p}_i(t)$, and the maximum strain-

498   rate deviation history, $\dot{p}_{\mathrm{dev}}(t) = \max \dot{p}_i(t) - \min \dot{p}_i(t)$, were calculated. The normalized

499   maximum strain-rate deviation history, $E_{\mathrm{dev}}(t)$, was then calculated as

$$E_{\mathrm{dev}}(t) = \frac{\dot{p}_{\mathrm{dev}}(t)}{\dot{p}_{\mathrm{mean}}(t)} \cdot 100\% \tag{14}$$

500

501   The time at onset of necking, t_{neck}, is defined as $E_{\mathrm{dev}}(t_{\mathrm{neck}}) = 20\ \%$. Fig. 18(b) illustrates the

502    $\dot{p}_i(t)$ and $\dot{p}_{\mathrm{mean}}(t)$ histories from the three elements in the quasi-static 600DL-S20 simulation

503   together with $\dot{p}_{\mathrm{mean}}(t_{\mathrm{neck}})$, while Fig. 18(c) display the $E_{\mathrm{dev}}(t)$ history and $E_{\mathrm{dev}}(t_{\mathrm{neck}})$ from the

504   same analysis. This approach to identify local necking has similarities with the experimental

505   approaches used in [13, 33]. The onset of necking is marked with a circle in Fig. 16 and Fig.

506   17. The simulations display a trend where onset of necking is either predicted close to the

507   experimental displacement at fracture or at a lower displacement. An exception is the

508   simulations of the 1400M-S150 tests where onset of necking is predicted at a significantly

509   larger displacement. The experimental onset of fracture is marked with a square in the

510   simulated force-displacement curves for the 1400M-S150 tests shown in Fig. 16 and Fig. 17.

511   Generally the predicted onset of necking in the simulations supports the experimental

512   findings. An exception is the 1400M-S100 tests, for which the experimental analysis was

513   inconclusive: strain concentration was observed in the DIC measurements, but local necking

514   was not observed from visual inspection (Fig. 13). The simulations indicate that necking

515   occurs before through-thickness shear fracture in these tests.

516   The equivalent plastic strain in the last image before failure is shown in Fig. 19. The image is

517   before incipient necking in all the simulations, except for the low-velocity and quasi-static

518   1400M-S150 simulations, where the last image before the experimental displacement at

519   fracture in the tests (marked with a square in the force-displacement curves in Fig. 16 and Fig.

520   17) are shown. Generally, the contour plots from the quasi-static and low-velocity simulations

521   are similar, although the low-velocity simulations display somewhat larger strains. The

522   contour plots in Fig. 19 resemble the experimental contour plots in Fig. 11, but the tendency

18

523   of a dominant strain concentration on one side of the centre of the specimen seen in the quasi-

524   static experiments is not observed in the simulations.

525   In order to gain information on the deformation histories at critical positions, the first and

526   second in-plane principal strains, ε_1 and ε_2, and the equivalent plastic strain-rate, $\dot{p}$, were

527   collected from the critical element in each simulation. The positions of the critical elements

528   are indicated with arrows in Fig. 19. Note that the first in-plane principal strain occurs along

529   the y axis and the second in-plane principal strain along the x axis of the coordinate system

530   given in Fig. 19. The simulated $\varepsilon_1 - \varepsilon_2$ curves are shown in Fig. 14. Here the points

531   corresponding to the displacement at fracture in the 1400M-S150 tests (marked with a square

532   in Fig. 16 and Fig. 17) are marked with squares in the 1400M-S150 simulations. Incipient

533   necking, as predicted by the applied necking criterion, is marked with a circle in each of the

534   other simulations. For the S20 and S100 geometries, good agreement between the

535   experimental and numerical strain paths is observed. For the S150 geometries, the numerical

536   strain paths for both materials are closer to equi-biaxial tension than the experimental strain

537   paths. Notably, the numerical strain paths are independent of the loading rate, while the low-

538   velocity experimental strain paths are closer to plane-strain tension than the quasi-static strain

539   paths. In general, the numerical models capture not only the global force-displacement

540   behaviour of the samples, but also the general trends of the local deformation histories at the

541   critical locations.

542   The strain-rate histories from a selected integration point in the critical element for each

543   simulation are shown in Fig. 20. Here a moving average filter was applied on the strain rate in

544   the 1400M simulations. Similar to Fig. 14, onset of necking is marked with circles, while

545   onset of fracture in the 1400M-S150 simulations are marked with squares. Since the point

546   with maximum strain-rate is moving during deformation, as illustrated in Fig. 10, the critical

547   elements experience a gradual increase in strain-rate up to necking. The average strain-rate up

548   to failure, $\dot{p}_{avg} = \Delta t^{-1} \int_0^{\Delta t} \dot{p}(t)\, dt$, where Δt is the time from incipient plastic strain to failure,

549   was calculated and the results are summed up in Table 5. The low-velocity impact tests have

550   an initial punch velocity 35000 times the punch-velocity in the quasi-static tests. As can be

551   seen from Fig. 20 and Table 5, the same scale factor applies reasonably well for the strain-rate

552   in the critical elements in the low-velocity and quasi-static simulations.

19

7 Concluding remarks

Low-velocity impact tests were conducted on sheets from the dual-phase steel Docol 600DL and the fully martensitic steel Docol 1400M. In addition, corresponding quasi-static tests were carried out as a reference. For both loading rates, the sheets failed under membrane loading and experienced stress states from uniaxial tension to equi-biaxial tension, thus covering important stress states that may occur during a generic impact situation. Generally the results in terms of force-displacement curves and strain histories at critical positions in the specimens were similar for low-velocity and quasi-static loading, independent of material and specimen geometry. This suggests that the quasi-static tests may give a good indication of the membrane failure of both materials in a generic low-velocity load case. All tests failed due to necking except for the martensitic steel sheet exposed to a nearly equi-biaxial loading. In this case, through-thickness shear fracture occurred without significant necking.

The finite element simulations were in good agreement with the experiments and supported the experimental finding that all tests apart from the martensitic sheet in a state close to equi-biaxial tension failed due to necking. Further, the in-plane principal strains and the equivalent plastic strain-rate were extracted from critical locations of the specimen in the finite element simulations. The evolution of the in-plane principal strains obtained numerically captured the general trends in the experimental results. The strain rates at critical locations in the tests were estimated in the range of 80-210 s^{-1} before failure for low-velocity loading and 0.002-0.005 s^{-1} before failure for quasi-static loading. Although adiabatic conditions prevail in the low-velocity tests, a material model which did not incorporate thermal effects provided good results in this study.

Acknowledgements

20

References

[1]   Langseth M, Larsen PK, Dropped objects' plugging capacity of steel plates: An experimental investigation. International Journal of Impact Engineering 1990;9(3):289-316.

[2]   Simonsen BC, Ship grounding on rock—I. Theory. Marine Structures 1997;10(7):519-562.

[3]   Paik JK, Pedersen PT, Modelling of the internal mechanics in ship collisions. Ocean Engineering 1996;23(2):107-142.

[4]   Marciniak Z, Kuczyński K, Limit strains in the processes of stretch-forming sheet metal. International Journal of Mechanical Sciences 1967;9(9):609-620.

[5]   Langseth M, Larsen PK, Dropped objects' plugging capacity of aluminium alloy plates. International Journal of Impact Engineering 1994;15(3):225-241.

[6]   Wen HM, Jones N, Experimental Investigation into the Dynamic Plastic Response and Perforation of a Clamped Circular Plate Struck Transversely by a Mass. Journal of Mechanical Engineering Science 1994;208(113):113-137.

[7]   Grytten F, Børvik T, Hopperstad OS, Langseth M, Low velocity perforation of AA5083-H116 aluminium plates. International Journal of Impact Engineering 2009;36(4):597-610.

[8]   Holmen JK, Hopperstad OS, Børvik T, Low-velocity impact on multi-layered dual-phase steel plates. International Journal of Impact Engineering 2015;78(0):161-177.

[9]   Alsos HS, Amdahl J, On the resistance to penetration of stiffened plates, Part I - Experiments. International Journal of Impact Engineering 2009;36(6):799-807.

[10]   Alsos HS, Amdahl J, Hopperstad OS, On the resistance to penetration of stiffened plates, Part II: Numerical analysis. International Journal of Impact Engineering 2009;36(7):875-887.

[11]   Simonsen BC, Lauridsen LP, Energy absorption and ductile failure in metal sheets under lateral indentation by a sphere. International Journal of Impact Engineering 2000;24(10):1017-1039.

[12]   Björklund O, Nilsson L, Failure characteristics of a dual-phase steel sheet. Journal of Materials Processing Technology 2014;214(6):1190-1204.

[13]   Hogström P, Ringsberg JW, Johnson E, An experimental and numerical study of the effects of length scale and strain state on the necking and fracture behaviours in sheet metals. International Journal of Impact Engineering 2009;36(10–11):1194-1203.

[14]   Stören S, Rice JR, Localized necking in thin sheets. Journal of the Mechanics and Physics of Solids 1975;23(6):421-441.

[15]   Jie M, Cheng CH, Chan LC, Chow CL, Forming limit diagrams of strain-rate-dependent sheet metals. International Journal of Mechanical Sciences 2009;51(4):269-275.

[16]   Walters CL, Development of a Punching Technique for Ductile Fracture Testing Over a Wide Range of Stress States and Strain Rates. 2009, Massachusetts Institute of Technology. p. 114.

[17]   SSAB. Docol 600DL. [cited 2014 05.01]; Available from: http://www.ssab.com/en/Brands/Docol1/Products/Docol-600-DL/.

[18]   SSAB. Docol 1400M. [cited 2014 05.02]; Available from: http://www.ssab.com/en/Brands/Docol1/Products/Docol-1400-M/.

[19]   Fagerholt E, Borvik T, Hopperstad OS, Measuring discontinuous displacement fields in cracked specimens using digital image correlation with mesh adaptation and crack-path optimization. Optics and Lasers in Engineering 2013;51(3):299-310.

21

627 [20] Chen Y, Clausen AH, Hopperstad OS, Langseth M, Application of a split-Hopkinson
628 tension bar in a mutual assessment of experimental tests and numerical predictions.
629 International Journal of Impact Engineering 2011;38(10):824-836.
630 [21] Albertini C, Montagnani M, Dynamic material properties of several steels for fast
631 breeder reactor safety analysis. Report EUR 5787 EN. 1977, Applied Mechanics
632 Division, Joint Research Centre: Ispra, Italy.
633 [22] Tarigopula V, Hopperstad OS, Langseth M, Clausen AH, Hild F, A study of
634 localisation in dual-phase high-strength steels under dynamic loading using digital
635 image correlation and FE analysis. International Journal of Solids and Structures
636 2008;45(2):601-619.
637 [23] Hershey AV, The Plasticity of an Isotropic Aggregate of Anisotropic Face-Centered
638 Cubic Crystals. Journal Applied Mechanics 1954;76:241-249.
639 [24] Logan R, Hosford WF, Upper-bound anisotropic yield locus calculations assuming -
640 pencil glide. International Journal of Mechanical Sciences 1980;22:419-430.
641 [25] Børvik T, Hopperstad OS, Berstad T, Langseth M, A computational model of
642 viscoplasticity and ductile damage for impact and penetration. European Journal of
643 Mechanics - A/Solids 2001;20(5):685-712.
644 [26] IMPETUS. www.impetus-afea.com. [cited 2014 10.04].
645 [27] Roth CC, Mohr D, Effect of strain rate on ductile fracture initiation in advanced high
646 strength steel sheets: Experiments and modeling. International Journal of Plasticity
647 2014;56(0):19-44.
648 [28] Clausing DP, Effect of plastic strain state on ductility and toughness. International
649 Journal of Fracture 1970;6(1):71-85.
650 [29] Dunand M, Mohr D, Hybrid experimental-numerical analysis of basic ductile fracture
651 experiments for sheet metals. International Journal of Solids and Structures
652 2010;47(9):1130-1143.
653 [30] Gruben G, Vysochinskiy D, Coudert T, Reyes A, Lademo O-G, Determination of
654 ductile fracture parameters of a dual-phase steel by optical measurements. Strain
655 2013;49(3):221-232.
656 [31] Hanssen AG, Auestad T, Tryland T, Langseth M, The kicking machine: A device for
657 impact testing of structural components. International Journal of Crashworthiness
658 2003;8(4):385-392.
659 [32] Handbook Es. [cited 2014 27.11]; Available from:
660 http://www.engineershandbook.com/Tables/frictioncoefficients.htm.
661 [33] Vysochinskiy D, Coudert T, Hopperstad OS, Lademo O-G, Reyes A, Experimental
662 detection of forming limit strains on samples with multiple local necks. Journal of
663 Materials Processing Technology;227:10.

664

Tables and figures

Table 1 Chemical compositions of the materials (in weight %) [17, 18].

Material	C	Si	Mn	P	S	Al_{tot}
600DL	0.10	0.40	1.50	0.010	0.002	0.040
1400M	0.17	0.20	1.40	0.010	0.002	0.040

Table 2 Lankford coefficients R_α and flow stress ratios r_α in uniaxial tension for two parallel tests in each direction ($\alpha = 0°,\ 45°,\ 90°$).

Material	$R_{0°}$	$R_{45°}$	$R_{90°}$	$r_{0°}$	$r_{45°}$	$r_{90°}$
600DL	1.06 / 1.05	0.94 / 0.92	1.22 / 1.17	1.00/1.00	0.99/0.99	0.99/0.99
1400M	1.01 / 1.02	1.30 / 1.21	1.08 / 1.15	1.00/1.00	0.97/0.97	1.00/1.00

Table 3 Constitutive model parameters for the two materials.

Material	σ_0 [MPa]	Q_1 [MPa]	C_1	Q_2 [MPa]	C_2	Q_3 [MPa]	C_3	$\dot{\varepsilon}_0$ [s^{-1}]	c	m
600DL	317.2	201.2	38.42	347.5	5.00	6000	0.01	$1\cdot 10^{-3}$	0.009	6
1400M	1200	253.6	773.5	97	135	200	6	$1\cdot 10^{-3}$	0.004	6

Table 4 Thickness in fracture zone, t_f, thickness 1.5 mm from fracture zone, $t_{1.5}$, and $t_f / t_{1.5}$ ratio.

Load	Geometry	600DL			1400M		
		t_f [mm]	$t_{1.5}$ [mm]	$t_f / t_{1.5}$	t_f [mm]	$t_{1.5}$ [mm]	$t_f / t_{1.5}$
Low-velocity	S20	0.72	1.28	0.56	0.47	0.88	0.54
	S100	0.75	1.21	0.62	0.75	0.89	0.84
	S150	0.65	0.98	0.66	0.58	0.72	0.80
Quasi-static	S20	0.76	1.19	0.64	0.39	0.89	0.44
	S100	0.69	1.20	0.57	0.70	0.91	0.77
	S150	0.61	0.91	0.68	0.60	0.68	0.88

675 Table 5   Average strain-rate up to failure in critical elements (in s^{-1}).

Loading	Low-velocity			Quasi-static		
Geometry	S20	S100	S150	S20	S100	S150
600DL	119	95	136	0.00339	0.00268	0.00395
1400M	78	126	208	0.00205	0.00298	0.00521

676

24
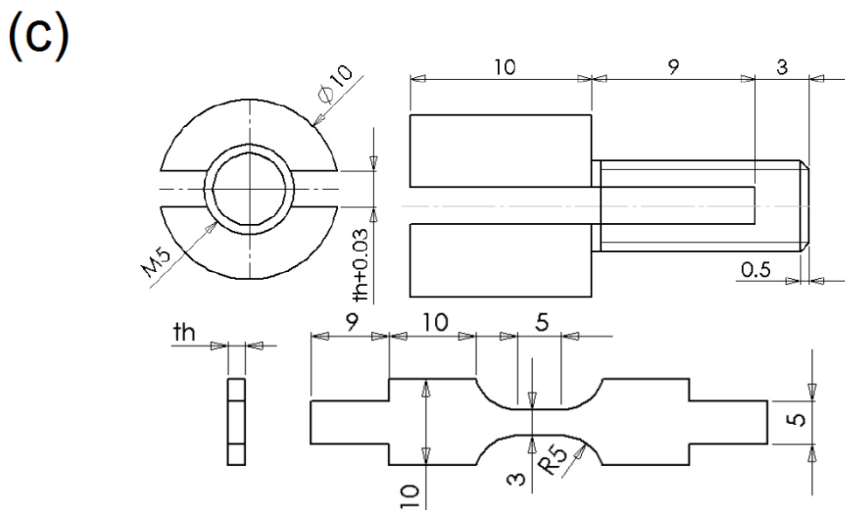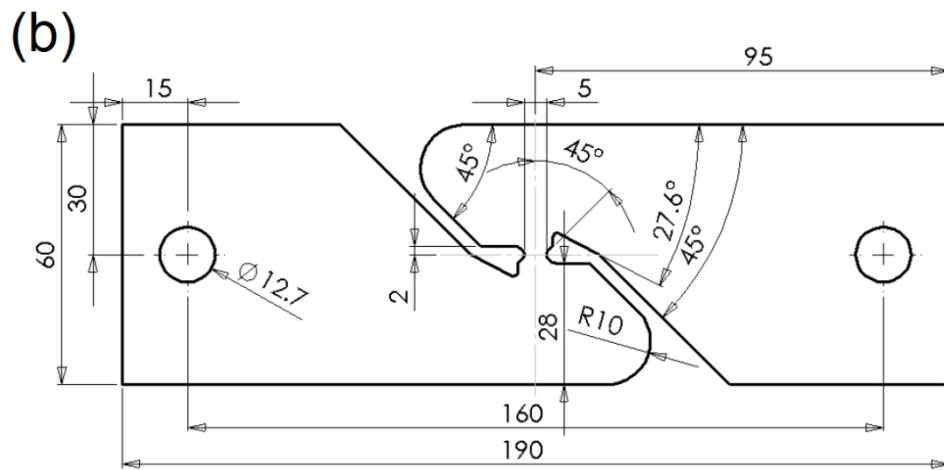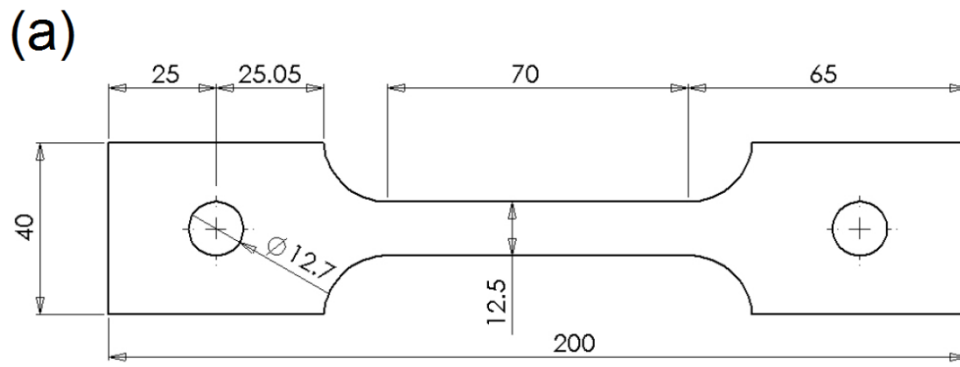
678   Fig. 1 Geometries of material test specimens: (a) uniaxial tension, (b) in-plane shear and (c)

679   uniaxial tension in split-Hopkinson tension bar.

680
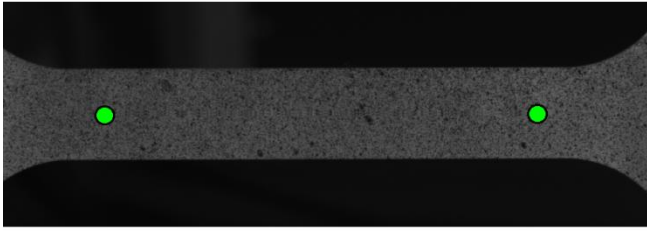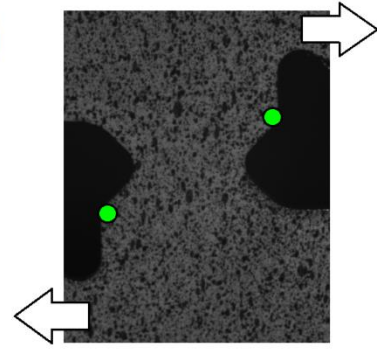
Fig. 2 Positions of the virtual extensometer for displacement measurements in (a) uniaxial tension tests and (b) in-plane shear tests. The loading direction of the shear test is indicated by arrows.

26

684
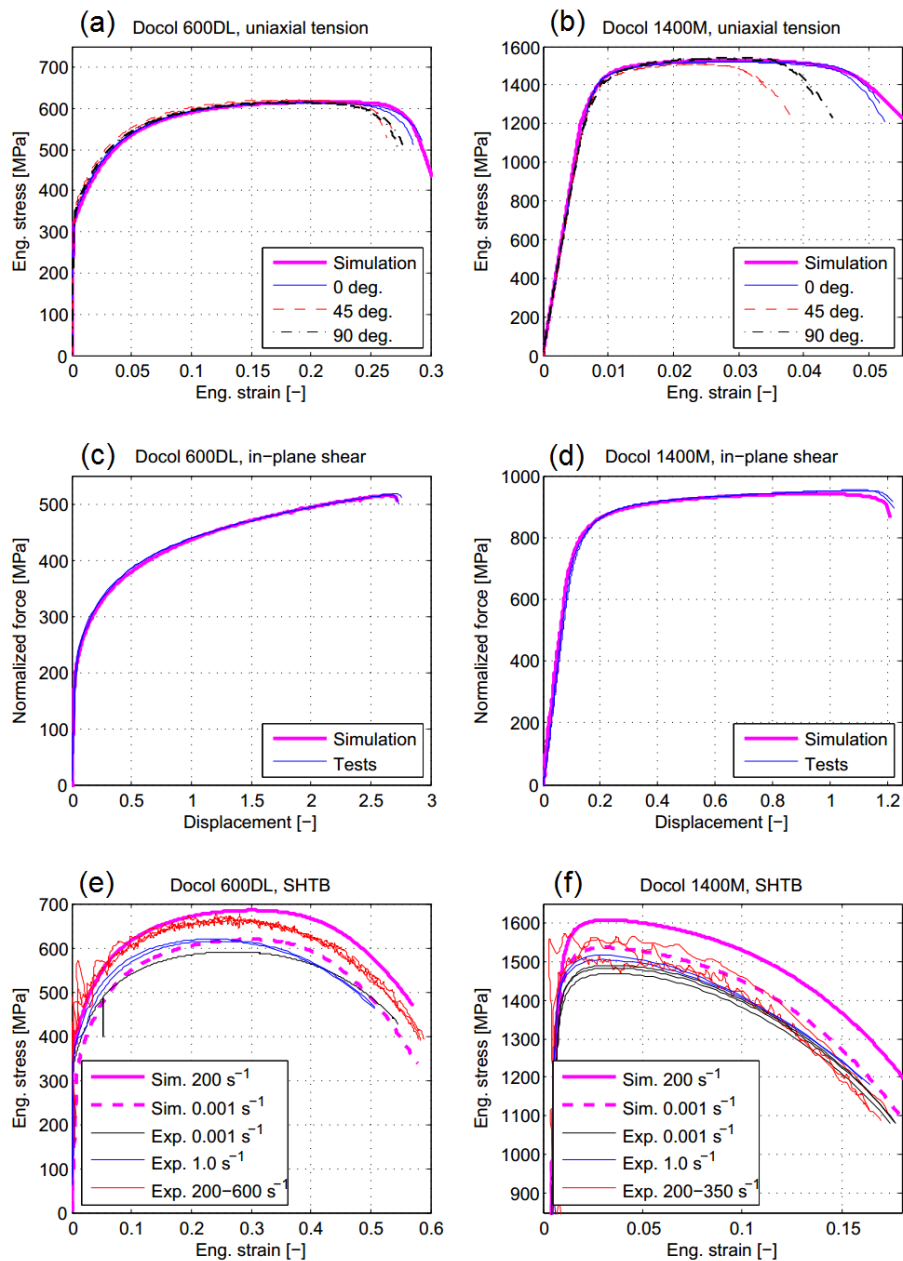
Fig. 3 Experimental and numerical quasi-static engineering stress-strain curves for (a) Docol 600DL and (b) Docol 1400M, experimental and numerical normalized force versus displacement curve in in-plane shear for (c) Docol 600DL and (d) Docol 1400M, and experimental and numerical engineering stress-strain curves from quasi-static and dynamic tests on small SHTB-type specimens for (e) Docol 600DL and (f) Docol 1400M

27
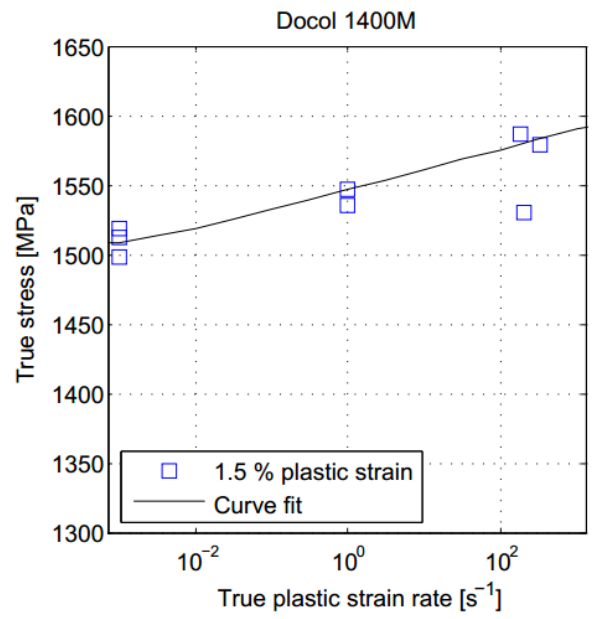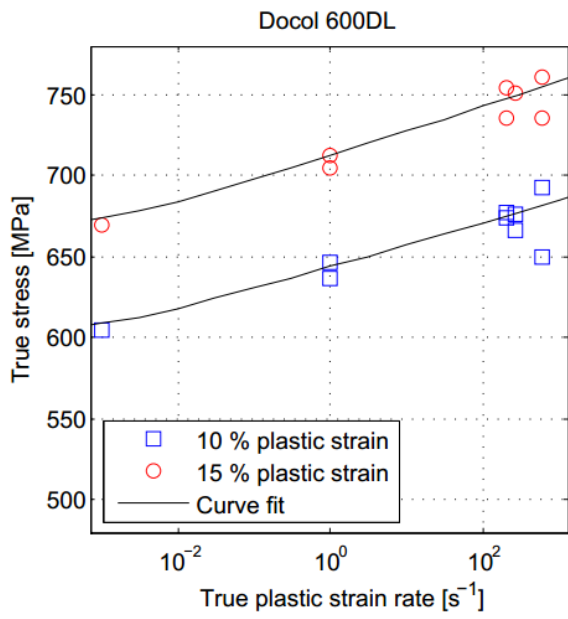
690

691   Fig. 4 Flow stress at various strain rates for the two steel sheets.
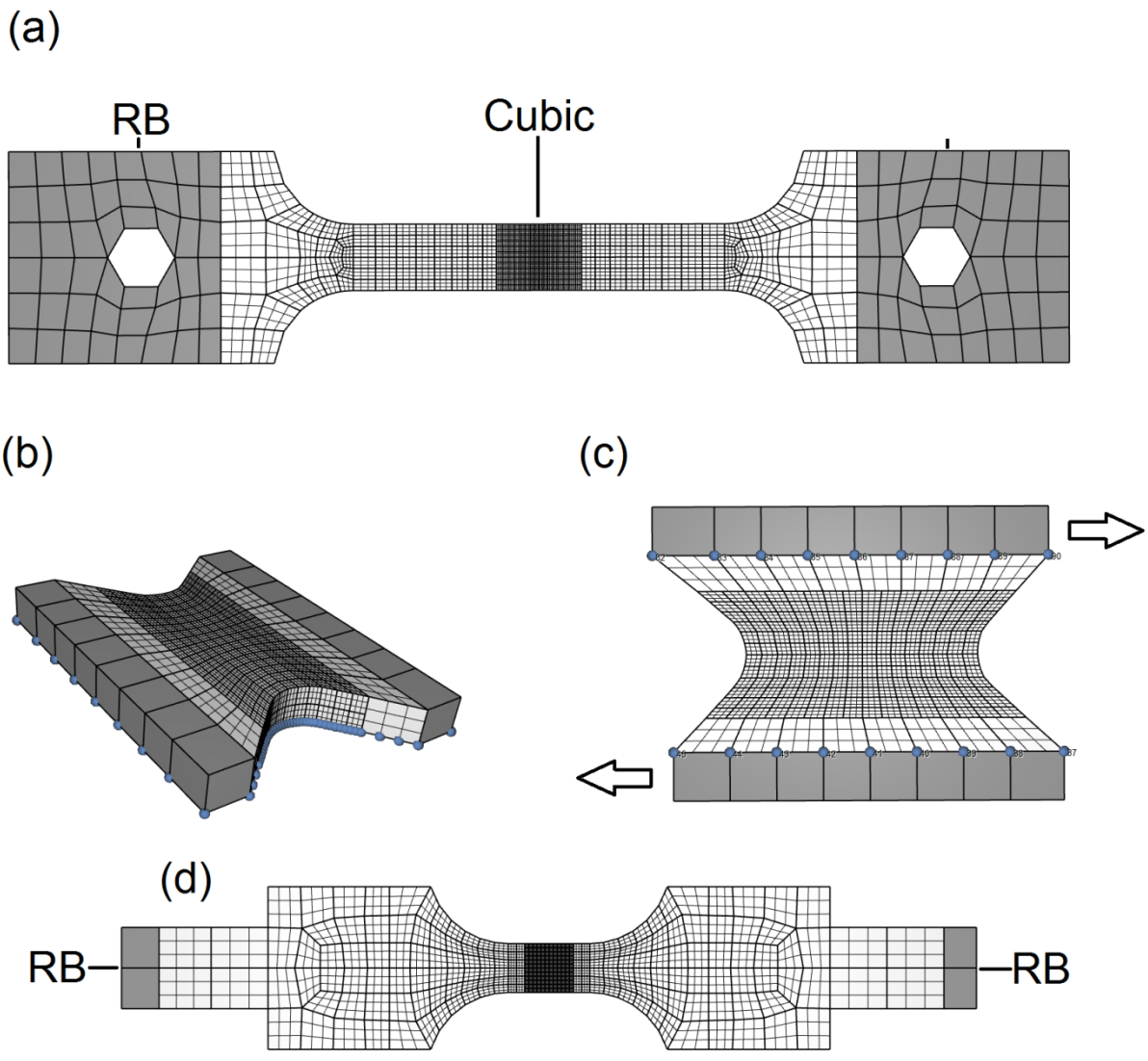
Fig. 5 Finite element models of material test specimens: (a) mesh of tensile specimen with cubic elements in the deformable part, a denser mesh in the region exposed to necking and rigid (RB) elements in parts with prescribed displacement, (b) mesh of shear specimen with nodes on the symmetry plane marked with dots, (c) mesh of shear specimen where nodes with prescribed displacement are marked with dots, and (d) mesh of SHTB specimen.

698
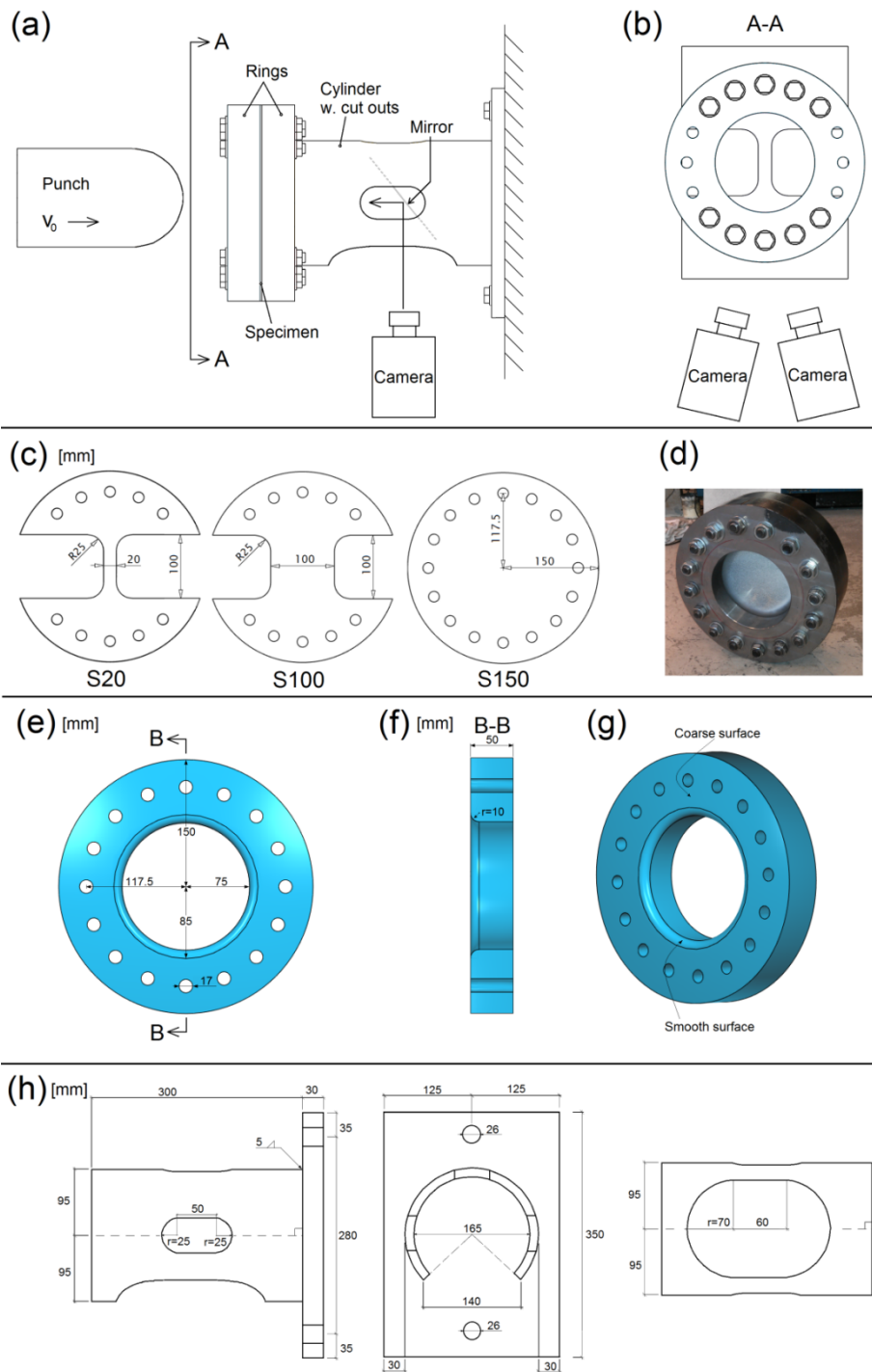
Fig. 6 Experimental set-up for the impact tests (in mm): (a-b) overview of the set-up from different angles, (c) specimen geometries, (d) specimen clamped to rings, (e-g) details of steel ring between specimen and cylinder (the steel ring closest to the punch has similar geometry, but without the rounded edge towards the specimen), and (h) details of the supporting cylinder and the mounting steel plate.
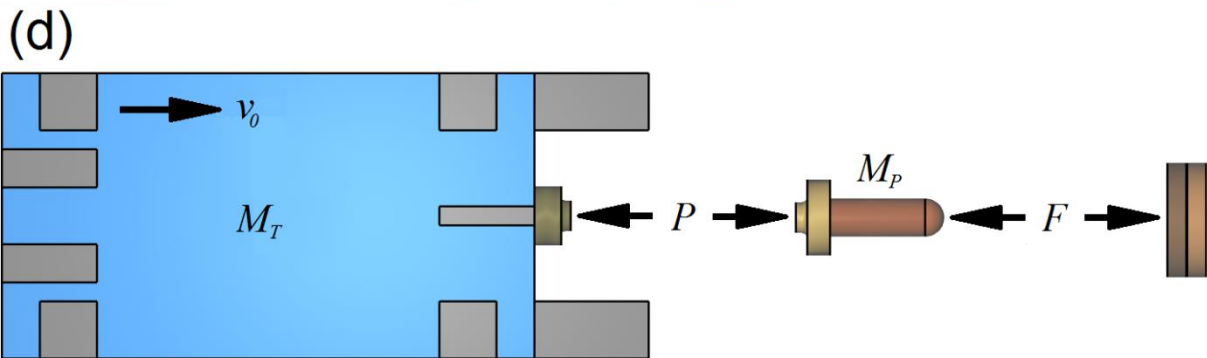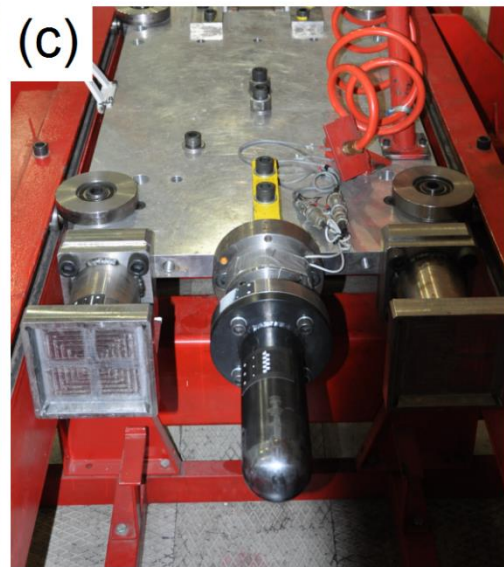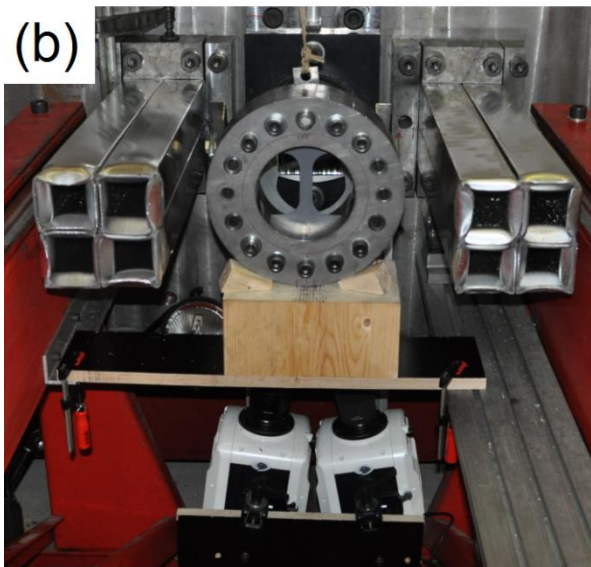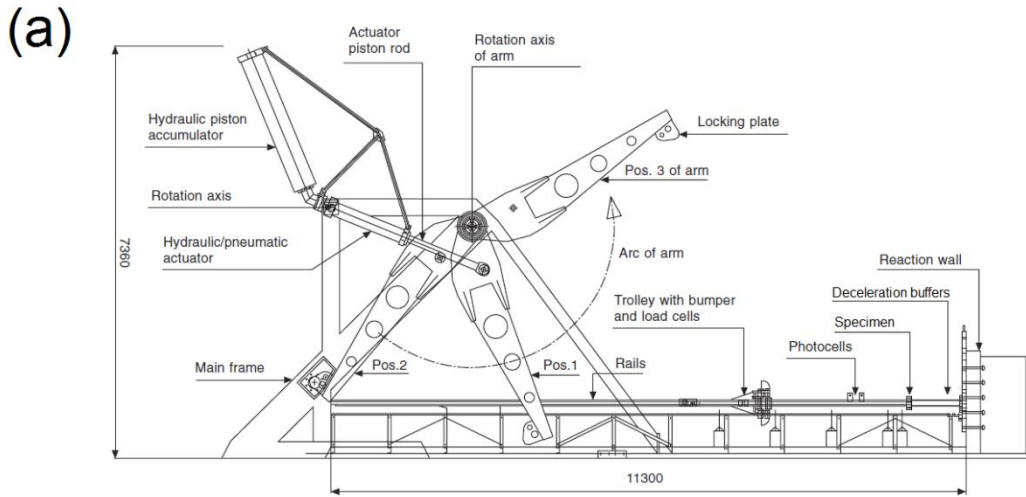
Fig. 7 Low-velocity impact tests: (a) pendulum impactor [31], (b) detail of specimen attached to brackets with high-speed cameras below and deceleration buffers on both sides, (c) close-up of the punch attached to the load cell and mounted on the trolley, and (d) schematic view of the set-up with forces acting in the load cell and between the punch and the specimen.

31
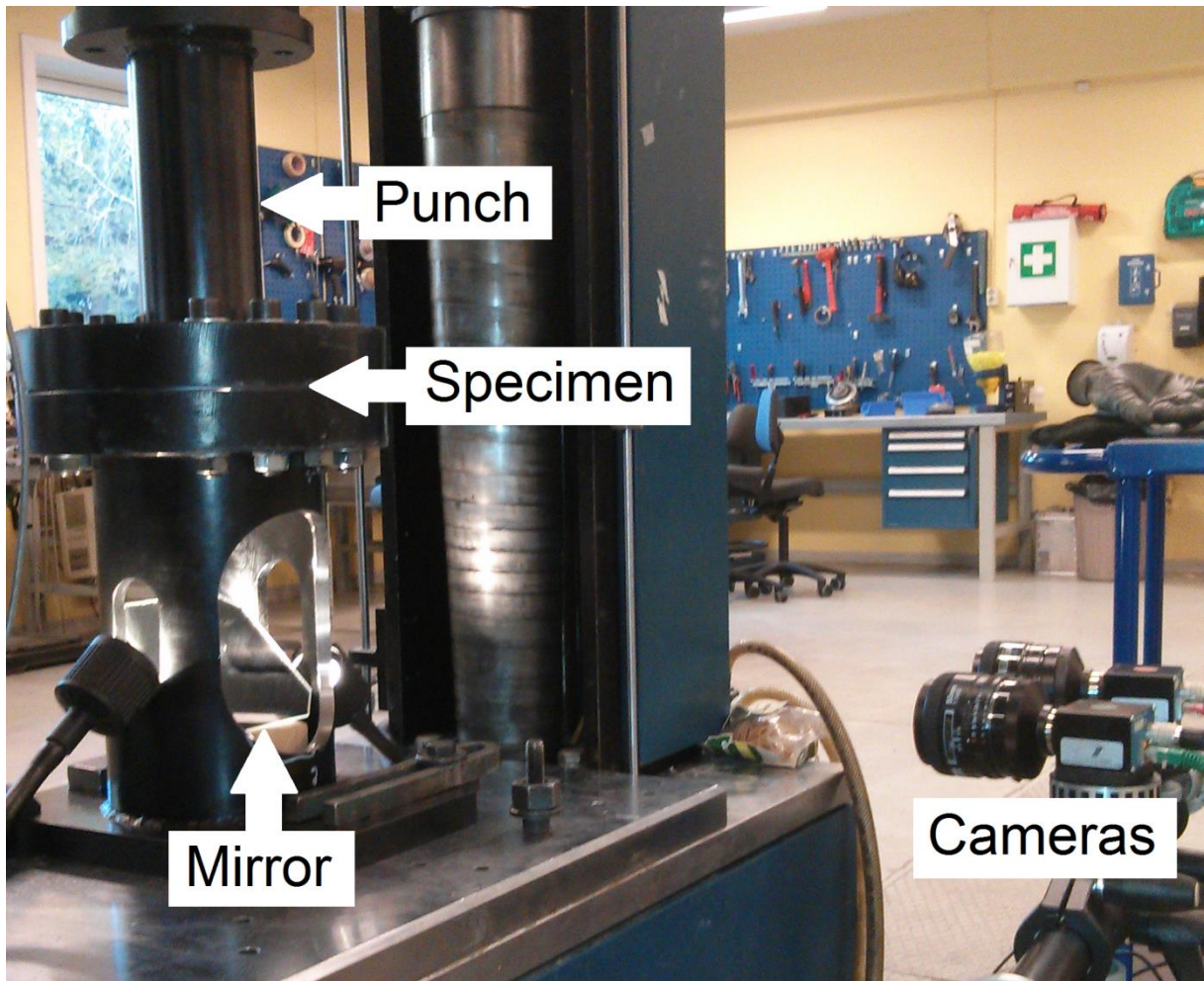
709

710   Fig. 8   Set-up for quasi-static testing.

711
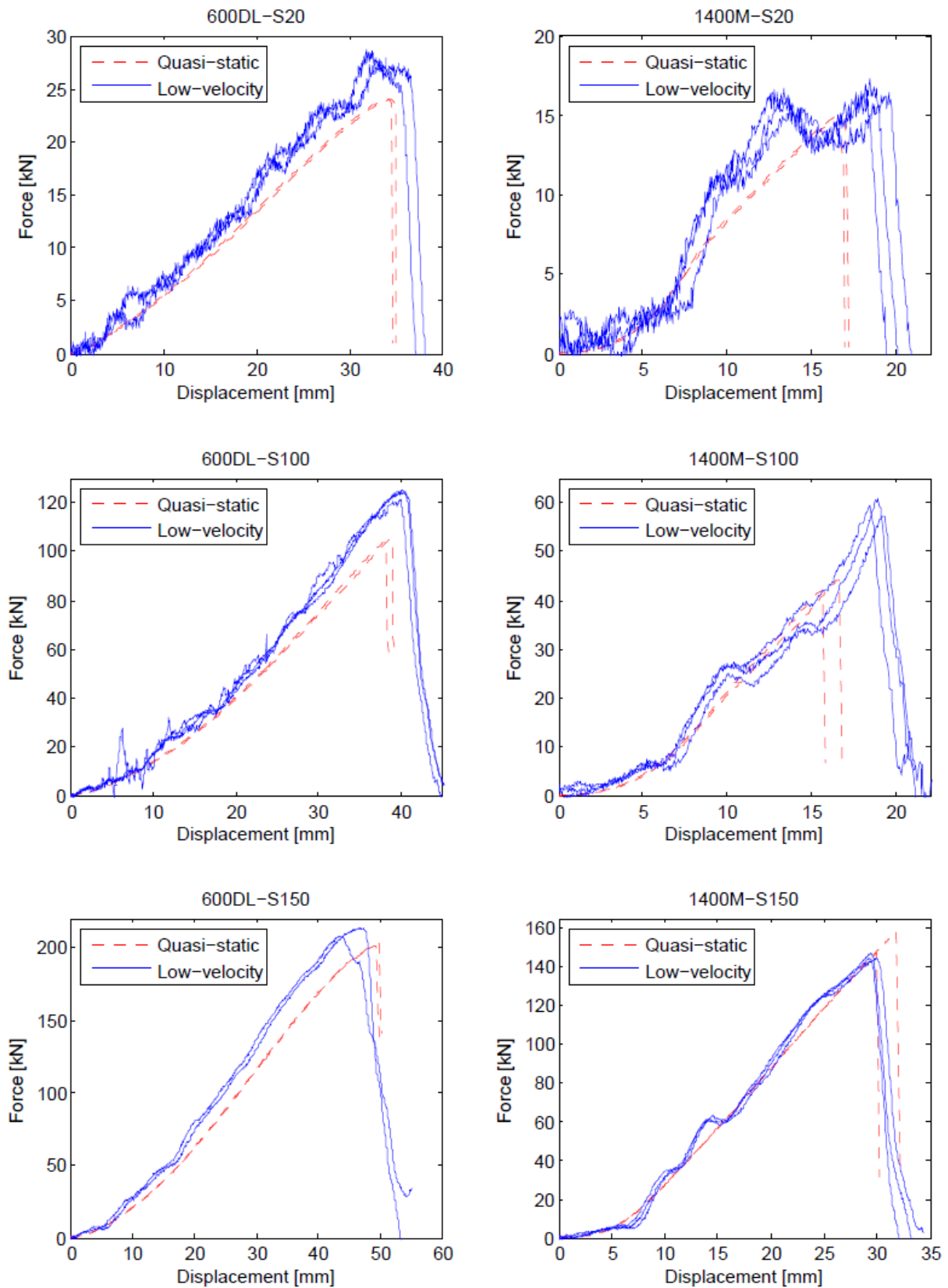
Fig. 9 Force-displacement curves from quasi-static and low-velocity impact tests. All
successfully completed tests are shown.
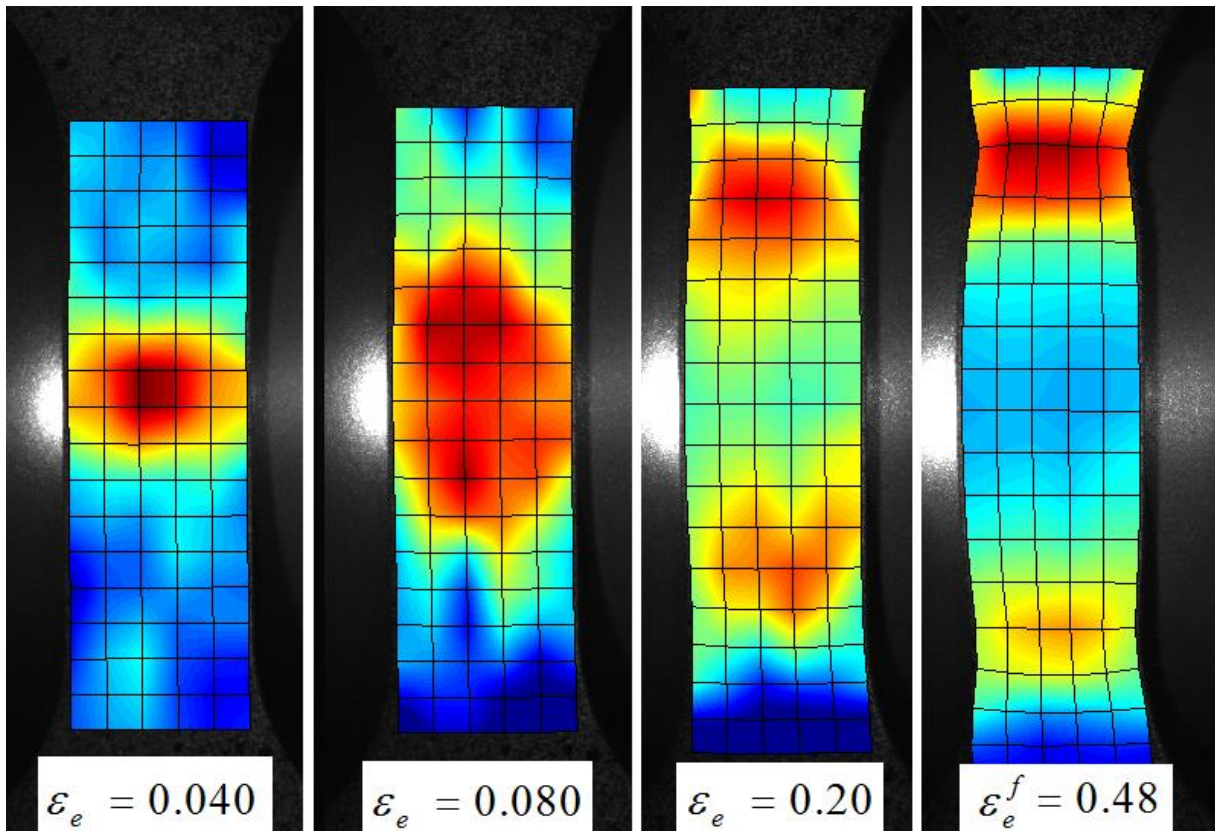
714

715   Fig. 10 Evolution of spatial strain distribution in one duplicate of the quasi-static 600DL-S20

716   test

717
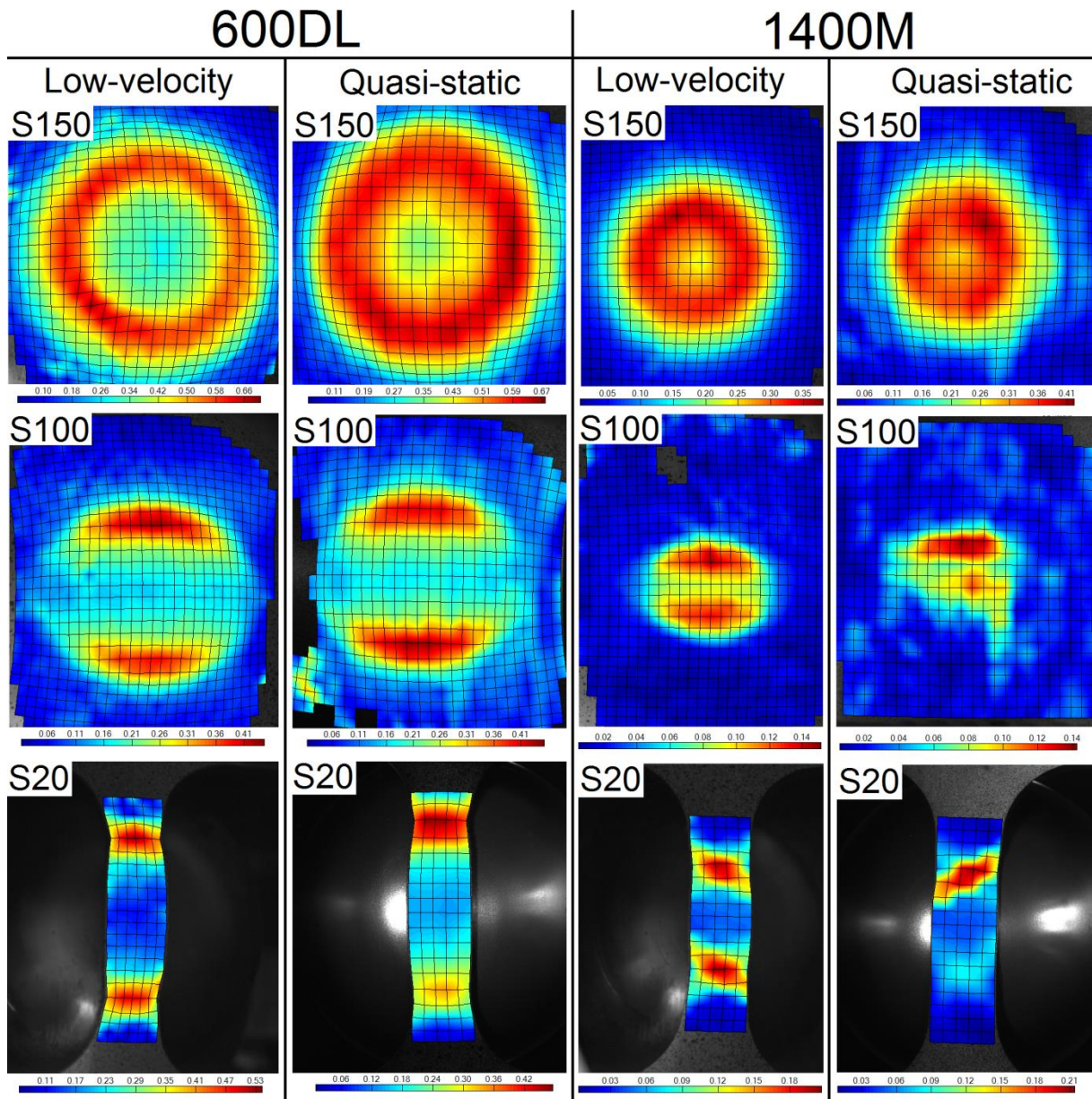
Fig. 11 Strain magnitude plots in the last image before fracture of selected duplicates of the low-velocity and quasi-static tests on Docol 600DL and Docol 1400M.
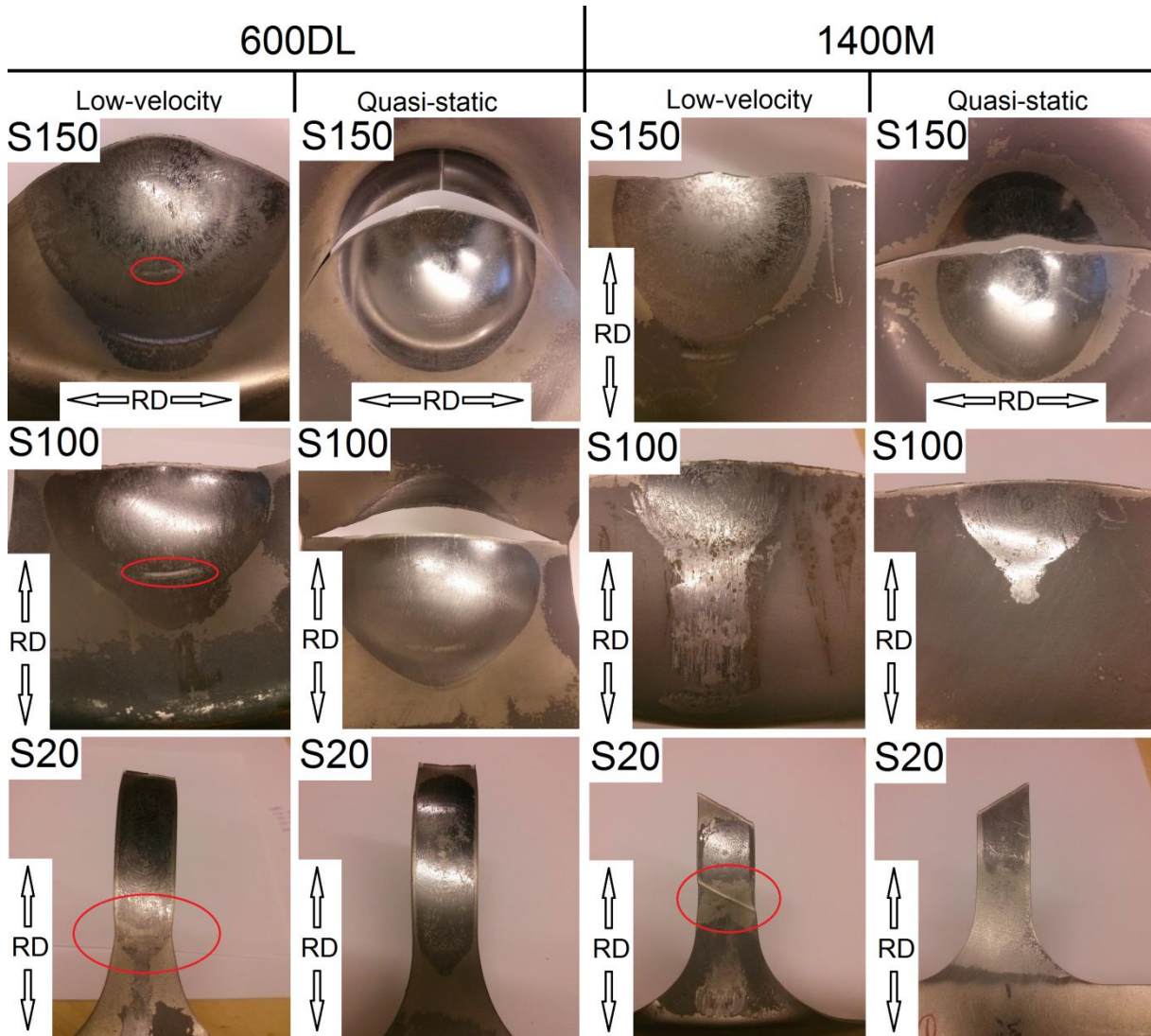
720

721   Fig. 12 Post-fracture images of selected duplicates of the sheet-impact tests.
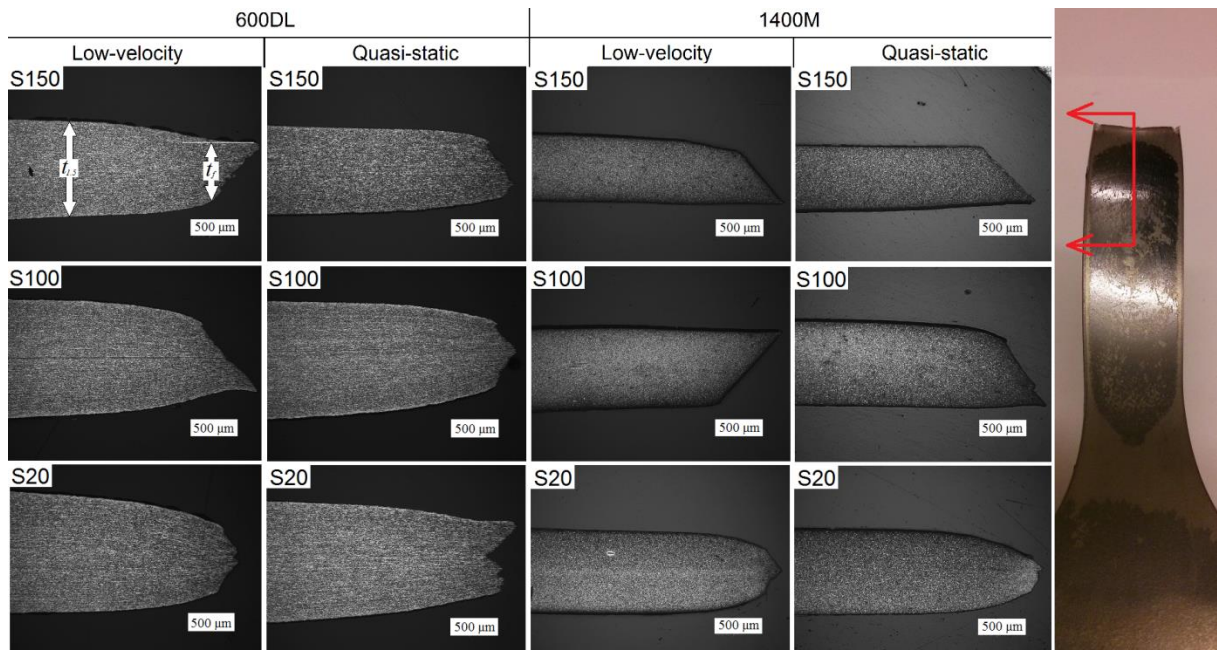
Fig. 13 Fracture zone profiles of selected specimens of the sheet-impact tests. The image to the right illustrates the position from where the fracture zone images are taken.
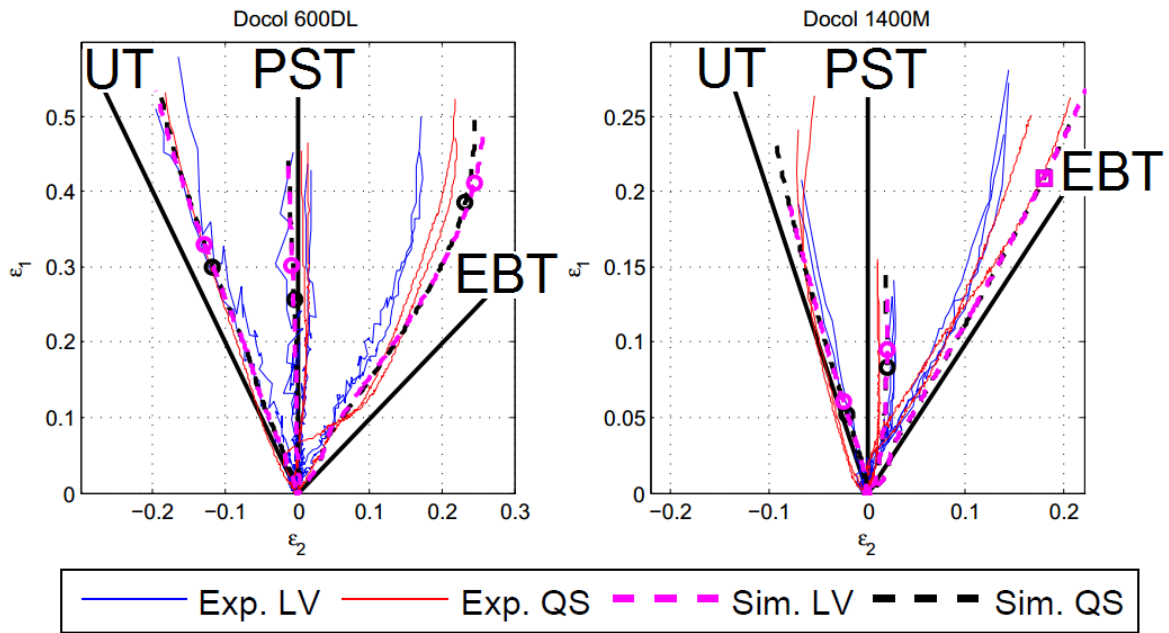
Fig. 14 Principal strain histories from DIC measurements and numerical simulations of low-velocity (LV) and quasi-static (QS) sheet-impact tests. The S20 geometry tests are close to uniaxial tension (UT), the S100 tests are close to plane-strain tension (PST), the S150 tests are close to equi-biaxial tension (EBT). The squares in the 1400M-S150 simulations correspond to the experimental displacement at fracture, while the circles correspond to incipient necking.

38
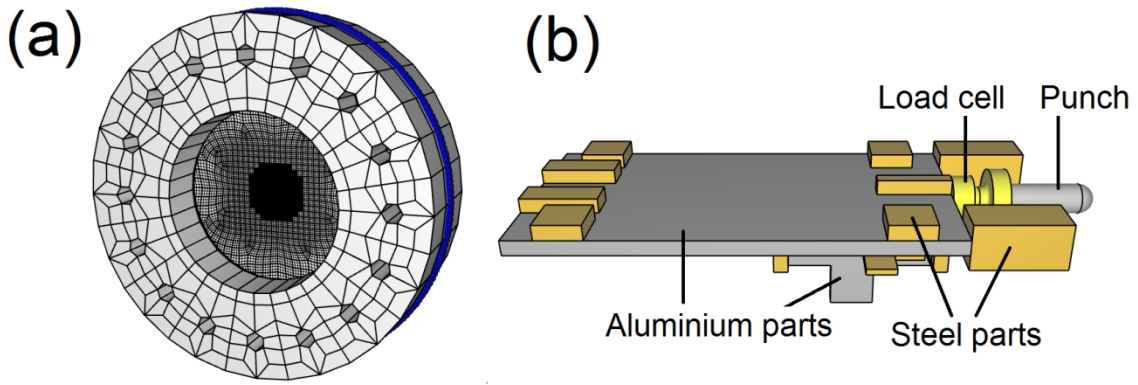
731

732 Fig. 15 Finite element (FE) model of low-velocity test set-up: (a) FE mesh of specimen

733 clamped between brackets. The nodes on the specimen with in-plane fixture are marked with

734 dots. (b) FE geometry of trolley, load cell and punch.
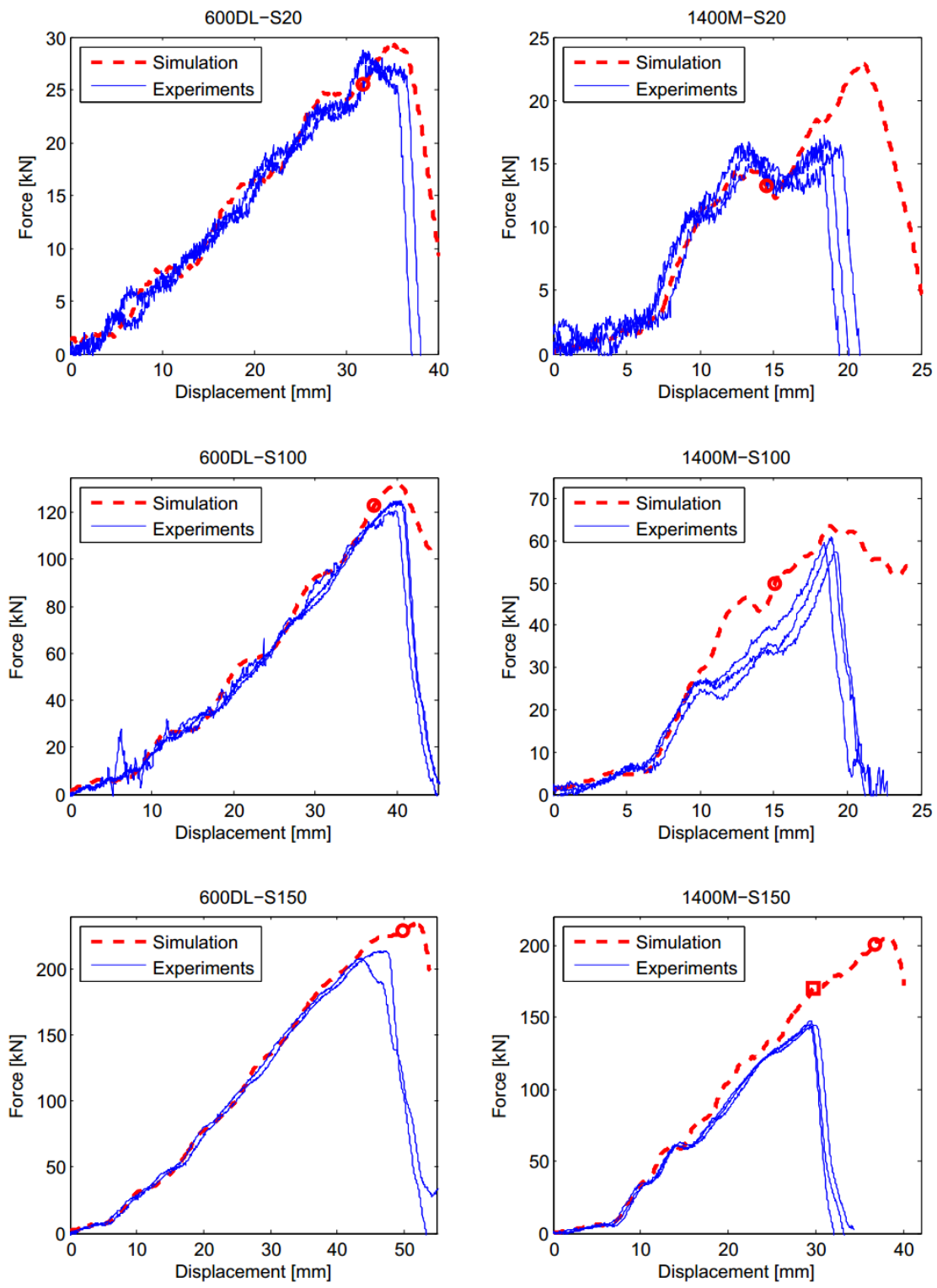
Fig. 16 Experimental and numerical force-displacement curves from low-velocity impact tests. Incipient local necking in the simulation is marked with a circle for each case. In the force-displacement curve for the simulation of the 1400M-S150 test, the square marks the displacement at fracture in the test.

40

740
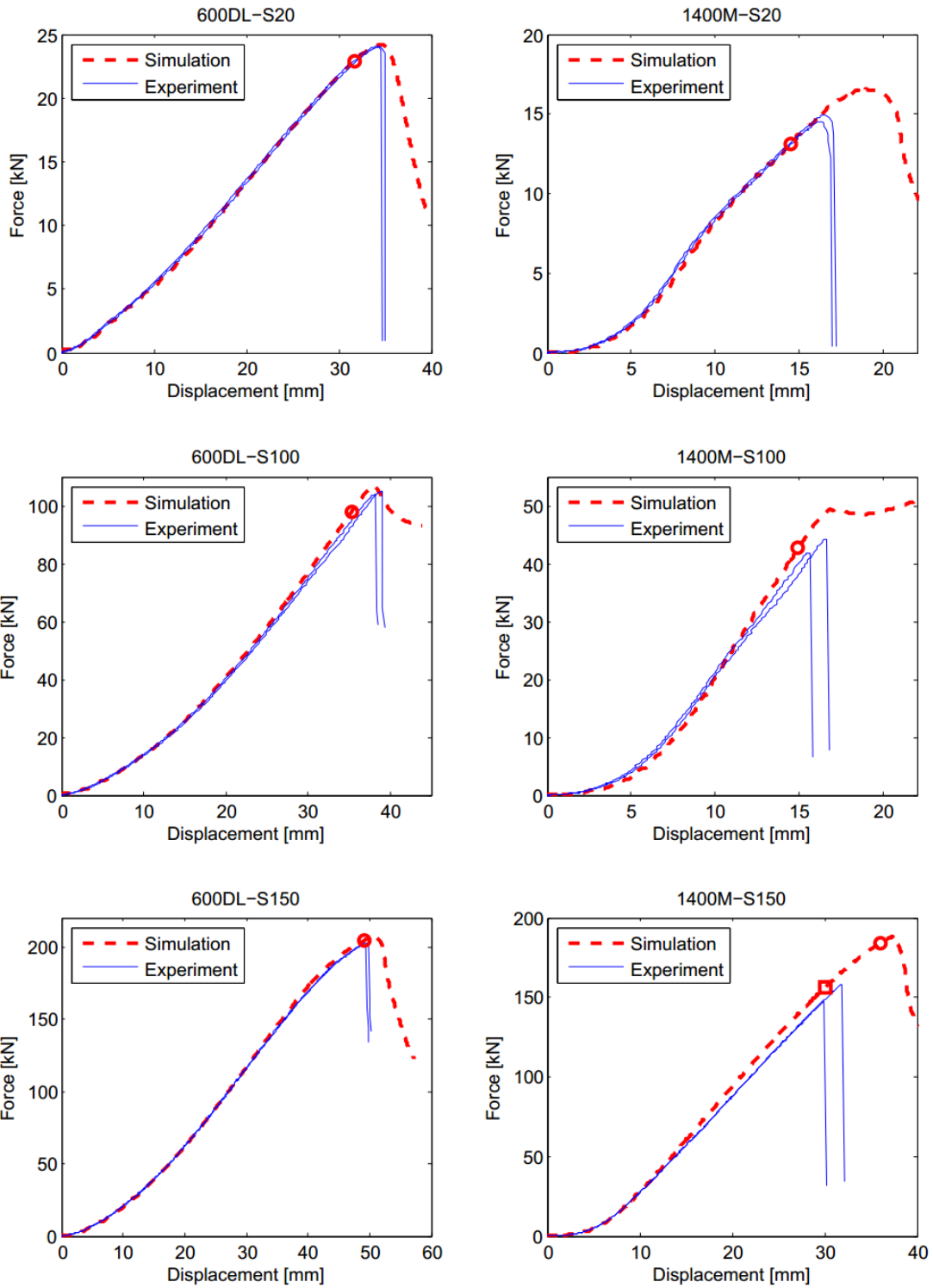
Fig. 17 Experimental and numerical force-displacement curves from quasi-static tests. Incipient local necking in the simulation is marked with a circle for each case. In the force-displacement curve for the simulation of the 1400M-S150 test, the square marks the displacement at fracture in the test.

41
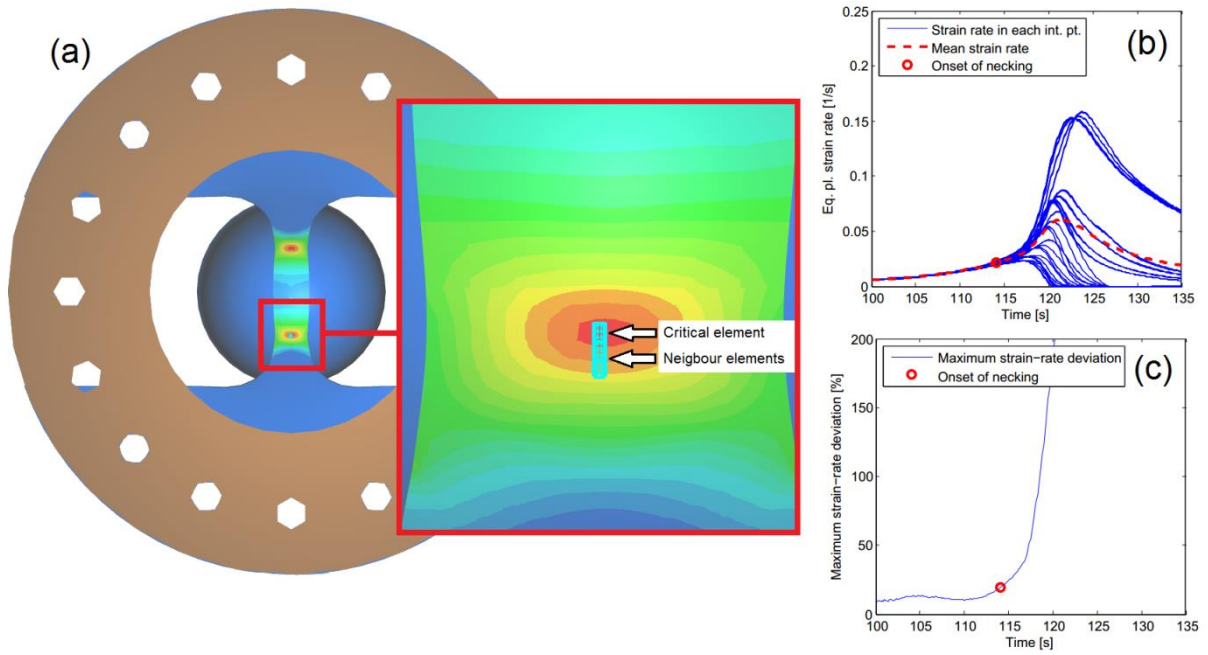
Fig. 18 (a) Equivalent plastic strain contours at $t = 117$ s in the quasi-static 600DL-S20 simulation and the locations of the critical and neighbouring elements. (b) Plots of $\dot{p}_i(t)$ and $\dot{p}_{\mathrm{mean}}(t)$ histories from the same analysis, and (c) the corresponding $E_{\mathrm{dev}}(t)$ history. The point of incipient necking is shown in (b) and (c).
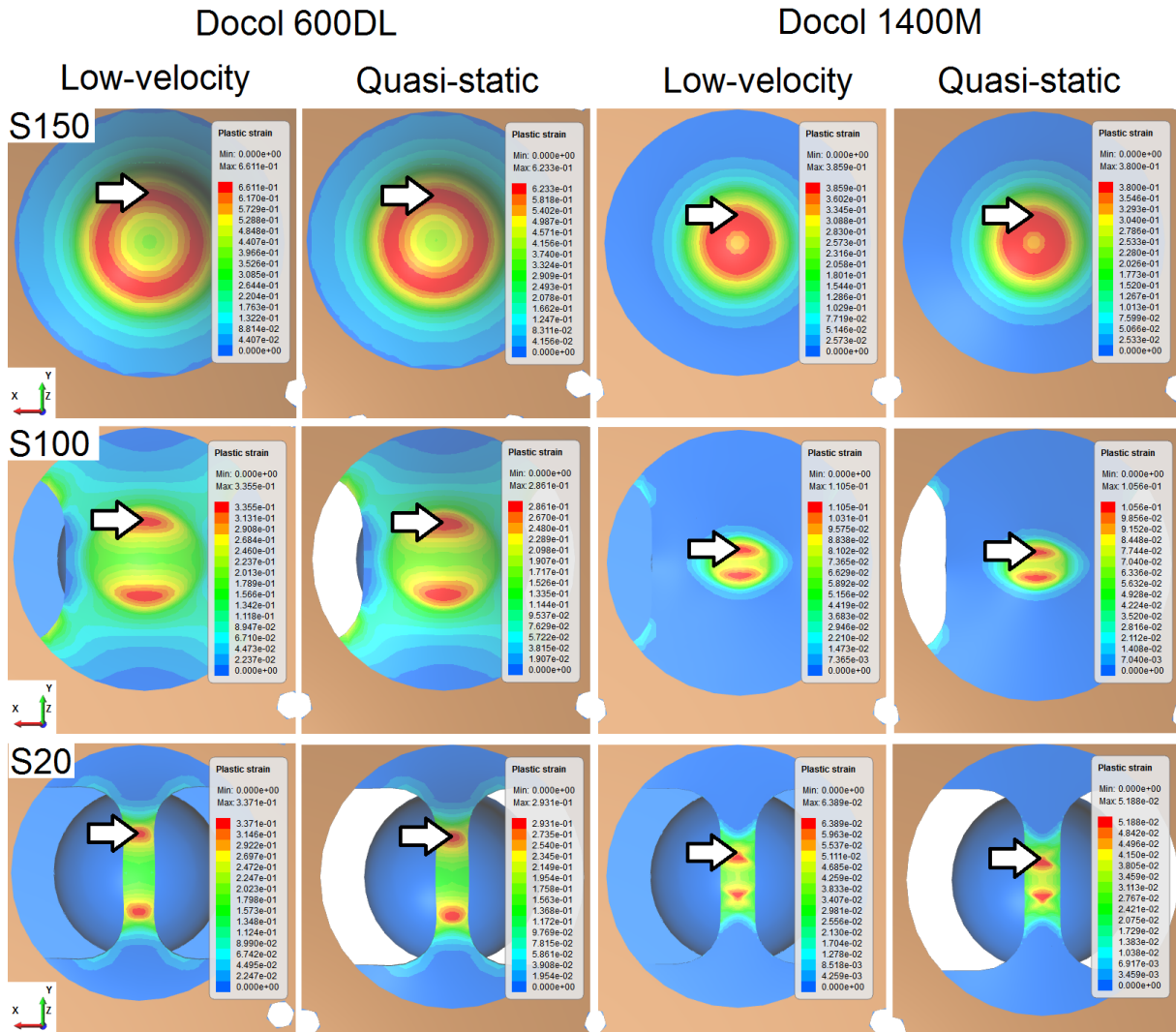
Fig. 19 Equivalent plastic strain in the last image before failure in the simulations of the sheet-impact tests. For the 1400M-S150 simulations, the image is taken before the displacement at fracture, while the other images are taken before onset of necking. The arrows indicate the positions where the largest deformations occurred.

43
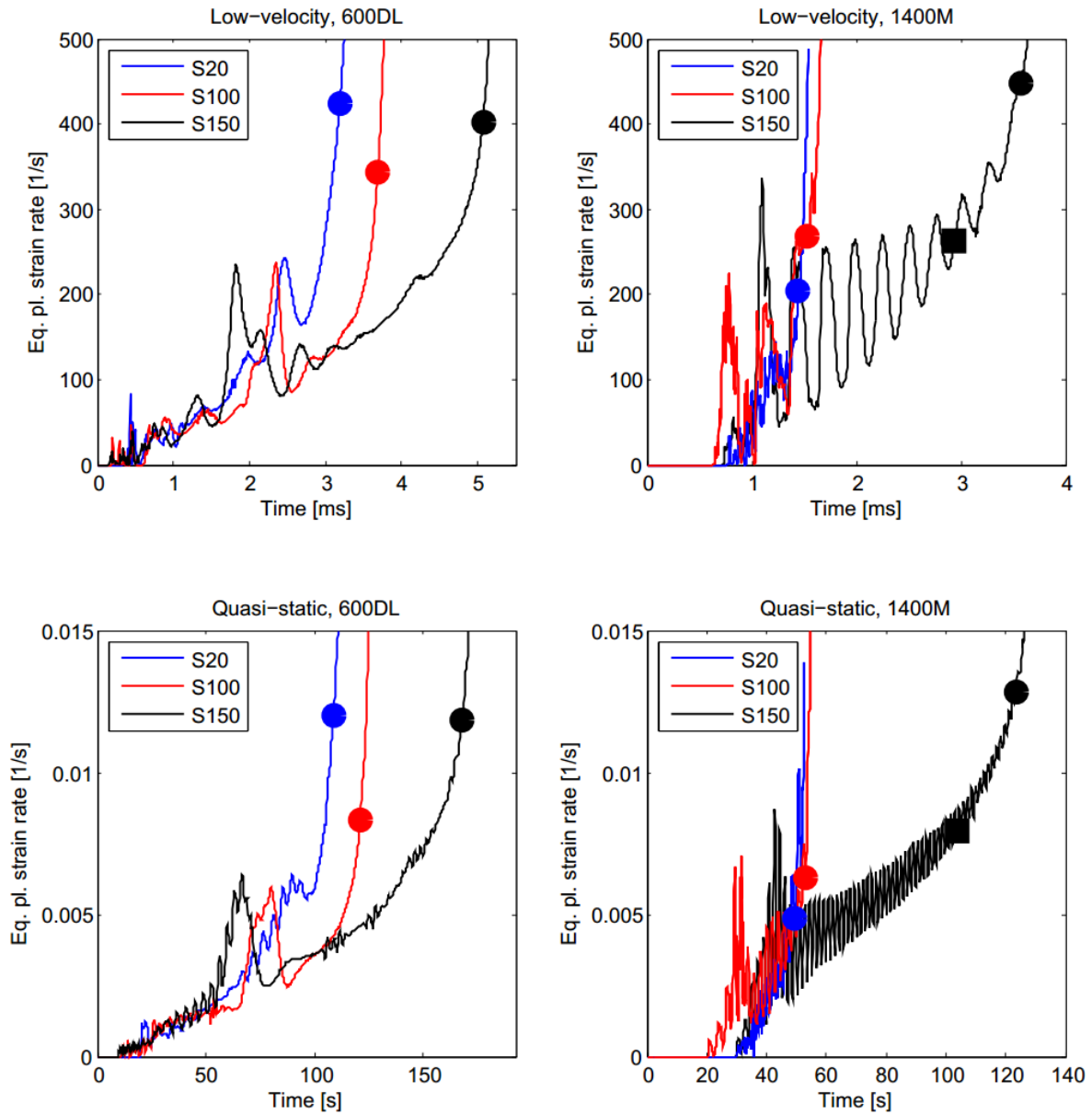
Fig. 20 Strain-rate history collected from critical elements in the simulations. Onset of necking is indicated with circles, while onset of fracture in the 1400M-S150 tests is indicated with squares.